



UNIVERSITÀ
DI PAVIA

SCUOLA DI ALTA FORMAZIONE DOTTORALE
MACRO-AREA SCIENZE E TECNOLOGIE

Dottorato di Ricerca in Scienze della Terra e dell'ambiente

Mattia Bonazzi

**Elastic geobarometry methods: validation through
synthesis and characterization of host-inclusion pairs
by means of Raman spectroscopy**

Anno Accademico 2018-2019
Ciclo XXXII

Coordinatore
Prof. Roberto Sacchi

Tutor
Prof. Matteo Alvaro

Co-tutor(s)
Prof. Simone Tumati

Contents

1	Preface	1
2	Introduction	5
I	Theoretical background	9
3	Elastic geobarometry for host-inclusion system	11
3.1	Isomeke	13
3.2	Relaxation	14
3.3	Geometry for anisotropic inclusion	17
4	Experimental petrology	20
4.1	Piston cylinder apparatus	22
4.2	Assembly	26
II	Solid-State synthesis	28
5	Introduction to solid-state synthesis	29
5.1	Experimental methods	31
5.1.1	Analytical techniques	36
5.1.2	Gel and glass preparation	36

5.2	Experiments with crystalline powder - YAG	37
5.2.1	YAG Sintering experiments at room P and T=1700°C .	40
5.2.2	YAG experiment with ruby at P= 3 GPa and T=1300°C	40
5.2.3	YAG experiment with Si and Ti metallic at P= 3 GPa and T ranging from 1000 to 1300°C	41
5.2.4	YAG experiment with diamond at P= 3 GPa and T= 1300 °C	42
5.3	Experiments with crystalline powder - pyrope	43
5.3.1	Diamonds in pyrope at P= 3 GPa and T=1300 °C . . .	46
5.3.2	SiO ₂ in pyrope at P= 3 GPa and T ranging from 1150 to 1200 °C	50
5.4	Experiments with non-crystalline powder at P= 3 GPa and T= 1200 °C	53

III Hydrothermal synthesis 56

6	Assessment of the reliability of elastic geobarometry with quartz inclusions	57
6.1	Abstract	57
6.2	Introduction	58
6.3	Methods	61
6.3.1	Piston-cylinder experiments	61
6.3.2	Sample quality assessment	62
6.3.3	Raman spectroscopy measurements	67
6.4	Results and discussion	68
6.4.1	Raman wavenumber shift, inclusion pressure and strain	68
6.4.2	Calculation of entrapment conditions	78

CONTENTS	iii
6.5 Conclusions	82
6.6 Supplementary materials	83
7 Conclusions	87
Bibliography	89

Chapter 1

Preface

The goal of my PhD project is to validate experimentally the elastic geobarometry method for elastically isotropic host-inclusion pairs. To this aim I focused on synthesizing host-inclusion pairs of mineral phases with known thermoelastic properties at well-defined and controlled P - T conditions. The residual pressures determined on these synthetic host inclusion pairs will provide the means for validating elastic barometry by comparison with those expected for inclusions entrapped at the chosen “artificial” entrapment P and T . The determined strain state of the inclusions by Raman spectroscopy allows us to determine the stresses components acting on the inclusions now from which we could calculate the residual pressure and in turn the entrapment pressure at the temperature conditions at which the synthesis were performed. The agreement between the determined entrapment pressures and those set during synthesis will confirm the reliability of the calculation of entrapment P - T as determined by means of elastic geobarometry. Also, the study of these inclusions provided me the possibility to investigate the effects of non-hydrostatic stresses on quartz inclusions in garnet at high-pressure (HP) metamorphic conditions (e.g. subduction, exhumation).

Chapter 2 (Introduction) is a brief introduction for the reasons and aims of my PhD project and its role into ERC project (grant agreement No 714936) by M. Alvaro.

First goal of this thesis is the synthesis of host inclusion pairs suitable to apply elastic method. The main concepts behind this project is how to determine the entrapment pressure for anisotropic inclusions trapped in isotropic host using elastic geobarometry method.

Part I (Theoretical Background) explains a state of art and theoretical principles of approach and methods that I used during my PhD project. Theoretical Background is divided in two parts:

Chapter 3 (Elastic geobarometry for host-inclusion system), in this chapter I explain the recent developments on the elastic methods to determine the entrapment pressure. In particular I focus on:

- Role of shape and position of inclusions in host;
- Issues and challenges in calculating the residual pressure;
- Backcalculation of the entrapment pressure (P_{trap}) from the residual pressure (P_{inc}) and effect of elastic relaxation.

Chapter 4 (Experimental petrology) in this chapter I explain how the experimental petrology reproduce the natural processes and in particular can play a fundamental role to validate for elastic geobarometry.

Part II (Solid-State synthesis) is composed by Chapter 5. It describes the solid-state experiments to synthesize a host inclusion pairs using sintering process.

Chapter 5 (Solid-state synthesis) reported all results that I obtained during development of new approach to synthesize a host inclusion pairs using

one monocrystalline rod as nucleation point to permit the epitaxial growth of powder (crystalline or not); as the single crystal, the rod, and the powder have the same chemical composition of rod. In our experiments, the material used as a host are synthetic YAG and a natural pyrope. The inclusions were inserted in the powder to be tapped inside the host.

All experiments were carried out in piston cylinder apparatus at the University of Milan.

Part III (Hydrothermal synthesis) is composed by Chapter 6. This part describes how we obtained quartz inclusions in garnet using hydrothermal method and explains the results obtained from elastic geobarometry on quartz inclusions.

Chapter 6 (Assessment of the reliability of elastic geobarometry with quartz inclusions), is the paper entitled “assessment of the reliability of elastic geobarometry with quartz inclusions” by Mattia Bonazzi, Simone Tumati, Jay Thomas, Ross J Angel, Matteo Alvaro.

This paper reported the results that I obtained by hydrothermal synthesis of quartz inclusions trapped in almandine garnet at eclogitic conditions in a piston cylinder apparatus, from which we determined the stress state in the inclusions by two methods.

The use of the hydrostatic calibration of the 206 and 464 cm⁻¹ lines of quartz lead to a large spread in inclusion ‘pressure’ values for inclusions trapped at 3 GPa, although 464 cm⁻¹ line is more accurate for inclusions trapped at 2.5 GPa. Entrapment pressures calculated with the hydrostatic calibrations can be up to 0.8 GPa in error.

The use of the mode Grüneisen tensors of quartz enables the full strain state and thus the stress state of inclusions to be determined, and leads to a much smaller spread in mean stress values inferred for inclusions, and the

calculated entrapment pressures differ from the known experimental values by less than 0.2 GPa. These results show that the most significant effect of the elastic anisotropy of quartz is on the Raman shifts of the inclusion, but not on the subsequent calculation of entrapment conditions. This paper was submitted to the Lithos on 9th April 2019, accepted on 9th September 2019 and In Press, Journal Pre-proof, Available online 10 September 2019.

Chapter 7 (Conclusions) is a summary of results obtained in this PhD Thesis and the possible future activities and projects related to the present PhD topics.

The convention adopted for this thesis is that the bibliography is placed at the end of the thesis. The bibliography of article is incorporated in that of the thesis.

Chapter 2

Introduction

An inclusion is one or more minerals or fluids that are trapped within a mineral (host). In Ultra-High-Pressure(UHP) rocks, inclusions are an important source of geological information. Elastic geobarometry makes use of the contrast in elastic proprieties between host and inclusion pairs to obtain the entrapment pressure of the inclusions which record the residual strain and stress. It is measured in the inclusion when its host is at ambient conditions. Subduction zones located at convergent plate margins are the major geodynamic sites that primarily affect plate tectonics and transport of crustal material deep into the Earth's mantle. Subduction of one tectonic plate below another plate is accompanied by deformation processes enhancing seismicity and by dehydration/melting of the subducting plate and overlying mantle, which affect magmatism and volatile (including greenhouse gas) recycling into magmas. However, the mechanisms attending the downwards transport of crustal material during subduction and its tectonic return back to the surface (exhumation) before and/or during continent-continent collisions are still poorly understood and controversial. This is because the history of subduction can only be obtained with the study of paleo-geological processes

by determining the pressure-temperature-time-depth (P - T - t - h) histories of Ultra-High-Pressure Metamorphic (*UHPM*) rocks that have been subducted to pressures greater than 3 GPa and subsequently exhumed to the Earth's surface. However, conventional thermo-barometry is severely challenged in *UHPM* terraines. For example, the same set of compositional data has been used to argue for a *UHPM* (O'Brien, 2008) and for a high T /low P origin for the granulites of the Bohemian massif (Štípská and Powell, 2005); the compositional gradients in minerals have in some cases led to interpretations 'boosted to the highest astonishment factor' (O'Brien, 2008). In the Dora Maira massif, a minimum P of 3 GPa is indicated by coesite inclusions in pyrope, whereas diamond-facies P of 4-4.5 GPa is claimed on the basis of experiments and thermodynamic modeling of phase assemblages. A fundamentally different method for geobarometry based on the elastic behavior of host minerals and their inclusions has been developed by our group (Angel et al., 2014a; Angel et al., 2015a; Angel et al., 2015b). The entire method is based on the observation that after entrapment, minerals trapped as inclusions within other host minerals will exhibit pressures that deviate from the external pressure because of the differences between the thermoelastic properties of the host and inclusion phases. This concept has been known for a long time (Rosenfeld and Chase, 1961) and has been applied extensively to interpreting the remnant pressures of inclusions in diamonds (e.g. Izraeli et al., 1999; Nestola et al., 2011; Howell et al., 2012). However, those results relied (Zhang, 1998) on the assumptions of linear elasticity (i.e. that the elastic properties of the host and the inclusion do not change with P and/or T). We have recently successfully incorporated non-linear elasticity (i.e. realistic equations of state) into the classic host-inclusion elasticity solutions for elastically isotropic systems (Angel et al., 2014a; Angel et al., 2015a;

Angel et al., 2015b). Our solution provides, from the measured remnant pressure of the inclusion, a line in P - T space of possible entrapment conditions called the entrapment isomeke along which the inclusion would experience the same pressure as the external pressure. The EosFit7 software suite (Angel et al., 2014b), which is provided free of charge to academic users from www.rossangel.net, now incorporates this calculation. However, this state-of-the-art in-situ elastic barometry that is based on isotropic elasticity still requires validation that must come from laboratory determination, before we apply it to natural metamorphic rocks. For example, we are fully aware that evidence for plastic flow is ubiquitous in *UHPM* rock units and may, in principle, wipe out evidence of pro-grade stress states. On the other hand, strain partitions into the weaker phases of the rocks, so strong phases like garnets may well preserve the stress fields around inclusions, in which case the stress fields of their entrapped inclusions will also be preserved. The goals of this thesis are:

1. Synthesized one or more inclusion minerals trapped in monocrystalline cubic host. for the eclogitic conditions, a common host-inclusion pairs can be garnet with quartz inclusions.
2. Demonstrated the validity of the numerous elastic geobarometry methods that are reported in literature (e.g. Schmidt and Ziemann, 2000; Angel et al., 2017; Murri et al., 2018 through the synthesis of host-inclusions system in laboratory.

We chose to carry out the syntheses following two approaches:

- **Solid-state synthesis** that consists to use monocrystalline garnet rods as seed crystals to permit the epitaxial growth of new garnet (Ikesue and Aung, 2006) which will also trap inclusion phases mixed into the

crystalline powder of the same compositions of seed. During the project after the preliminary results we decided to move on and change the type of powder from crystalline to non-crystalline. The advantage of solid-state synthesis is the fine control on the size and position of the inclusions and then permit us to measure the inclusions using X ray single crystal diffraction and Raman Spectroscopy.

- **Hydrothermal synthesis** that consists of a oxide mixture plus water at eclogitic conditions (e.g. Thomas and Spear, 2018; Bonazzi et al., 2019. From this starting material will crystallize free single crystals of garnet with a lot of small inclusions, and also other minerals, immersed in fluid. The advantage of this approach allows us to measure several inclusions in different host that are obtained from same experiment. From these syntheses we will provide a statistical information on reliability of elastic measurements on inclusions.

Part I

Theoretical background

The theoretical background is divided in two chapter. In the first chapter I summarized the fundamental concept of the elastic geobarometry for host inclusion system. The second chapter I explained the relevance of experimental petrologist to investigate the natural processes and how to apply it at the validation of elastic geobarometry through the synthesis of host inclusion pairs.

Chapter 3

Elastic geobarometry for host-inclusion system

One main goal of metamorphic petrologists is to reconstruct the P - T paths about the history of rocks using chemical equilibrium of between two mineral phases. However, the application of conventional thermobarometry methods can be strongly challenging in many rocks due to alteration process, chemical re-equilibration and diffusion, and kinetic limitations. As alternative at conventional thermobarometry it is that to investigate the P - T conditions using elastic geobarometry method that is independent of chemical equilibrium (e.g. Rosenfeld and Chase, 1961; Enami et al., 2007; Angel et al., 2015a; Anzolini et al., 2018; Murri et al., 2018). The elastic geobarometry is method that uses the difference in their elastic proprieties of host and inclusion pairs to determine entrapment conditions during mineral growth. An inclusion is a mineral that trapped into other mineral (host).

The fundamental assumption is that at the moment of entrapment both minerals host and inclusion are at the same pressure (P) and temperature (T) conditions and the inclusion perfectly fills the cavity in the host (e.g. Goodier,

1933; Eshelby, 1957 Fig. 3.1). Up to when the entrapment conditions remain the same, also the host-inclusion pairs will show the same P - T conditions. However, if P - T change and the host and the inclusion have a contrast in elastic proprieties, they will exhibit different volume changes. The elastic proprieties of minerals are described by elastic tensor or equation of state.

For examples upon exhumation to the surface, if inclusion is softer than the host, it will develop strain and stress field that will be different to those of the host because the volume of the host cavity will expand less than inclusion. As consequence, the inclusion is constrained by the host to a smaller volume than it should have if inclusion were free. This concept has been known for a long time (Rosenfeld and Chase, 1961) and has been applied extensively to interpreting the remnant pressures (or residual pressures) of inclusions in diamonds (e.g. Izraeli et al., 1999; Nestola et al., 2011; Howell et al., 2012). However, those results relied (Zhang, 1998) on the assumptions of linear elasticity; that the elastic properties of the host and the inclusion do not change with P or T . Recently it was successfully incorporated non-linear elasticity (i.e. realistic equations of state) into the classic host-inclusion elasticity solutions for elastically isotropic systems (Angel et al., 2014a; Angel et al., 2015a; Angel et al., 2015b). The solution provides, from the measured remnant pressure of the inclusion, a line in P - T space of possible entrapment conditions called the entrapment isomeke along which the inclusion would experience the same pressure as the external pressure. Isomekes can be determined using EosFit7 package (Angel et al., 2014b) that now incorporates this solution. At this point comes into play the other parameters that is necessary to determine real remnant pressure of inclusion and its is relaxation (see paragraph 3.2). From residual or remnant pressure (P_{inc}) using equation of state (EoS) we back calculate the entrapment conditions

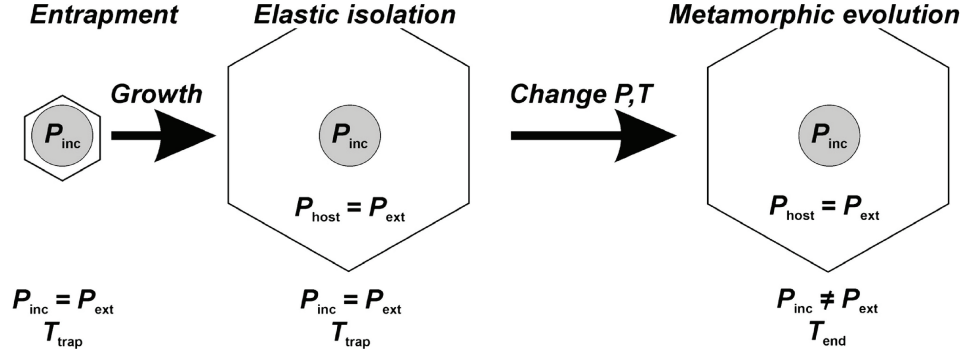


Figure 3.1: Sketch of inclusion entrapment into host. During the entrapment and growth of the host, the pressure (P) and temperature (T) for host and inclusion remains equal at the external conditions. The inclusions deviate the pressure from external conditions only when the external pressure change and if inclusion is elastic isolated in the host by Angel et al. (2015a)

(P_{trap}). At present an important limit of elastic method is that can be used only when all changes in the host-inclusion system are occurred under elastic deformation.

3.1 Isomeke

All crystals change their volume at change of pressure and temperature. The volume change $\left(\frac{\delta V}{V}\right)$ for a single mineral phase depends by thermal expansion coefficient (α) and volume compressibility (β):

$$\left(\frac{\delta V}{V}\right) = \alpha \delta T - \beta \delta P$$

And this behavior is described by isochor, that is a curve graphing temperature against pressure, when the volume of the substance is held constant. For free host(H) the isochor is defined as:

$$\left(\frac{\delta V}{V}\right)_V = \alpha \delta T - \beta \delta P$$

This condition is valid only to one phase, then it cannot be applied to host-inclusions system. Because as I already explained before in previous paragraph, after entrapment the volume of the hole in the host and the volume of the inclusion change in a different way following their elastic proprieties. Then we need to introduce an idea proposed by Rosenfeld and Chase (1961) and subsequently called isomeke by Adams et al. (1975). Isomeke is defined as a line in P - T space that represents conditions under which the host (H) and inclusion(I) pairs have the same volumes (Fig. 3.2).

$$\left(\frac{\delta P}{\delta T}\right)_{(V_I-V_H)} = \frac{\alpha_I - \alpha_H}{\beta_I - \beta_H}$$

The isomeke concept can be used to determine residual pressure on inclusion (Angel et al., 2014b). Now if we image moving along the isomeke from entrapment conditions (P_{trap} and T_{trap}) to the final temperature T_{end} . At final state the stress in the inclusion and the host is uniform and equal to the external pressure, which it is called P_{foot} . This calculation is made without any influence of the geometry of the system. But the isothermal decompression causes a mechanical disequilibrium in both minerals. Consequently, the stresses are readjusted through the relaxation process (Angel et al., 2014b).

3.2 Relaxation

During the exhumation on surface, for inclusion softer than host we have that the volume of inclusion change more of the volume host. Therefore, the inclusion shows a volume smaller volume than expected for the external pressure and temperature conditions, because its expansion will be stopped by host. The volume change of the host and inclusion are calculated using EoS (Angel et al., 2014a). The pressure P_{thermo} for inclusion that is calculated

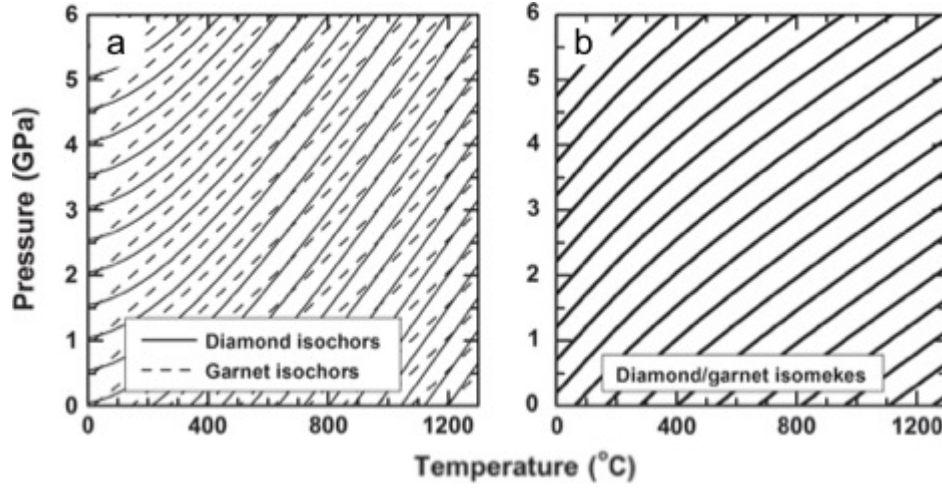


Figure 3.2: (a) The isochors for diamond and garnet that are calculated from their equations of state. (b) The isomekes of garnet inclusion in diamond are parallel to the isochors when the isochors of the two minerals are parallel to one another.

directly from equations of state of inclusions while the host is under the external pressure ($P_{H,end}$), so $P_{thermo} > P_{H,end}$. This calculation show is a physically problem because inclusion and host are under unstable “virtual” state. There is a difference in radial stress between host/inclusion wall. This effect generates an expansion of inclusion on the wall of host increasing the radial stress in the host adjacent to the inclusion and an part of stress in the inclusion is relaxed ($\Delta P_{I,relax}$). The expansion of the inclusion continues until the radial stress in the inclusion is the same of the host adjacent to the inclusion while stress gradient in the host decreases until the external stress at the outside surface of the host (Goodier, 1933; Eshelby, 1957). So the residual pressure of inclusion $P_{I,end}$ is given by two parts:

$$P_{inc} = P_{thermo} + \Delta P_{I,relax}$$

The first part of equation P_{thermo} can be calculated from the EoS of the two phases ($P_{thermo} > P_{inc}$). The problem is to estimate the second part of equations, (Angel et al., 2014b) proposed a new relaxation expression ($\delta P_{I,relax}$):

$$\Delta P_{I,relax} = \varepsilon_H K_{21}$$

The relaxation is calculated from the volume change ε_H and form K_{21} that indicate the elastic interaction between elastic proprieties of host inclusion pairs:

$$K_{21} = \frac{K_I - K_H}{K_I - \frac{4}{3}G_H}$$

For small pressure is possible consider K_{21} constant and this is the unique approximation used to obtain $\Delta P_{(I,relax)}$ value (Angel et., 2014b). The relaxation can be calculated also in terms of pressure to P_{foot} way and this second approach is that used into GUI program EosFit-Pinc (Angel et al., 2017). Following Bower (2009) the equation that determine final volume change of inclusion can be described in terms of finite changes in pressure as:

$$\varepsilon_I = \varepsilon_H + \frac{3(P_{inc} - P_{end})}{4G_H}$$

P_{inc} and P_{end} are the pressure of inclusion and host at the final P_{foot} pressure Angel et al. (2017). Using this formulation there are no assumptions about elastic properties of the material inside the inclusion, and there are no assumptions of linear elasticity (which would mean constant values of K_H and G_H). Because the force balance is calculated for the final conditions, the value of G_H to be used is that at the final conditions with the host under the external pressure change dP_{ext} . The unique assumption used here is that G_H does not change as a result of the deviatoric stresses that develop in the

host around the inclusion (e.g. Eshelby, 1957; Zhang, 1998; Howell et al., 2010). P_{inc} is found by the same equations using iterative cycle, and then the entrapment isomeke can be calculated using the EoS of the two phases (Angel et al., 2017).

3.3 Geometry for anisotropic inclusion

In natural system, the anisotropic inclusions in isotropic host can have several shapes or can be close to the surface or to other inclusions. As logical consequence, many authors have asked whether all these possible differences influence the calculation of P_{trap} ? Current isotropic models of elastic geobarometry assumes that inclusions must be spherical and isolated at the center of host and to obtain the real entrapment conditions (Eshelby, 1957; Zhang, 1998; Mazzucchelli et al., 2018; Campomenosi et al., 2018). Then the results of P_{inc} will be different for non-rounded shape of inclusions. Recent numerical models showed the effect of deviations from ideal geometry, including the size of the inclusion relative to the host and its proximity to external surfaces. The geometries modeled are ellipsoids with aspect ratios 2:1:1, 1:2:2, 5:1:1, and 1:5:5. For each model, we performed calculations by means of several elastic isotropic properties for the host and the inclusion to investigate potential scaling laws. From finite elements (FE) simulation is defined a geometrical factor (Γ) that normalized the deviation of recorded pressure for non-ideal inclusion from that expected for an ideal isolated spherical inclusion:

$$\Gamma = \frac{P_{inc}^{non-ideal}}{P_{inc}^{ideal}} - 1$$

For example, always using FE simulation is calculated that the deviation

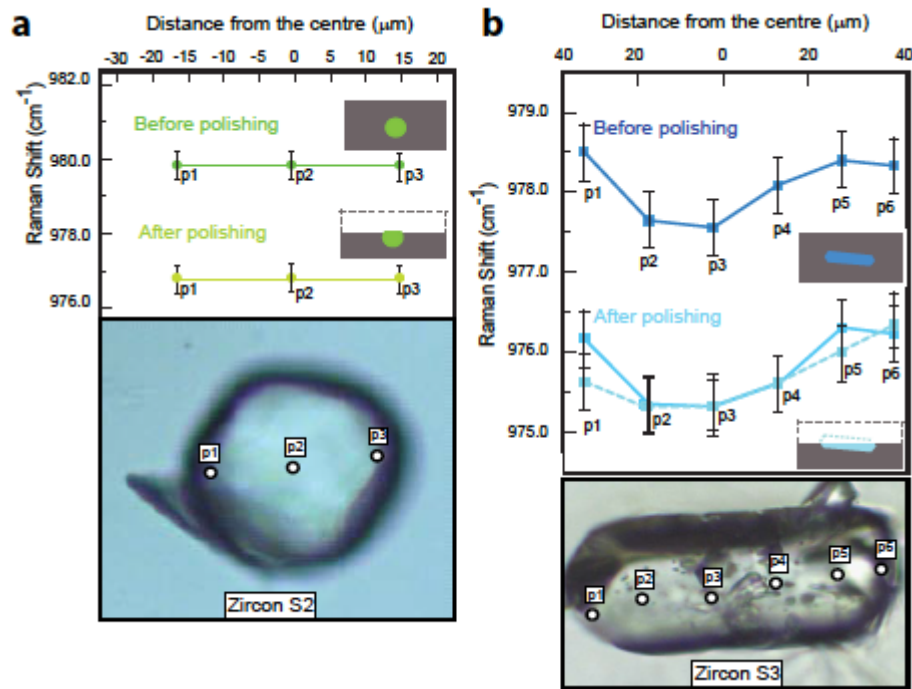


Figure 3.3: (Raman shift of 975 cm^{-1} wavenumber in zircon inclusion with a rounded (a) and an idiomorphic (b) shape before and after the final step of polishing. The solid lines in dark green and blue show the Raman shift before the polishing; the solid line in light green and blue show the Raman shift dashed line in b traces the data points measured after two days of final exposure of the grain.

for soft platy inclusions in a stiff host as quartz in garnet with (aspect ratio 1:5:5) in P_{inc} is greater than 7%. For isotropic elasticity, FE simulations showed that 'isolated' inclusion means that it has to be at least 3 radii from external surfaces or other inclusions. Recently Campomenosi et al. (2018) demonstrated using Raman spectroscopy that P_{inc} is homogenous only in rounded inclusion while it changes along a faceted inclusion (Fig. 3.3). These results are completely agreement with theory proposed by Eshelby (1957) and numerical models of Mazzucchelli et al. (2018). Therefore, on inclusion with non-ideal shape we can obtain a correct P_{inc} from the Raman shifts. The measurements have to collect at the center of inclusion and then calculated P_{inc} must be corrected for grain shape using geometrical correction Mazzucchelli et al. (2018).

Chapter 4

Experimental petrology

Experimental petrology is a branch of petrology that reproduce in laboratory the physical and chemical conditions under which rocks have formed in nature (e.g. Edgar and Edgar, 1973; Shaw, 2018). In particular this approach is used to investigate compositions and processes that occur inside of the Earth. This sector of petrology is fundamental because the informations of Earth's interior are limited. We can directly obtain information using drilling (few km), or through xenolites that are fragments of rock or mineral transported on surface by magma inside the Earth. The experimental petrology is a tool that does not solve the petrological problems, but it adds further data to determine the genesis of rocks. Thus, the experimental petrology is complementary with field studies. It is necessary to clarify that some assumptions on limitations of experimental petrology results. First, experimental system are simplified by chemical and physical point of view compared to natural systems. Second, the determination of thermodynamic equilibrium is often difficult to establish because the thermodynamic functions for determination of equilibrium are well known for many minerals at room P and T but even today some functions are lacking at high pressure

and temperature (in the last years, many studies are solving this problem). This problem is explained by Fyfe (1960). Third, that size and reaction time of samples are shorter about 10^6 and 10^{10} than in nature, also these problems are explained by Fyfe et al. (1958) and Fyfe (1961). These limitations are obvious and common for all experimental laboratory. In modern laboratory, we can divide the type of experiments according to equipment required to produce the pressure and temperature conditions of formation of the rocks in nature. Following this classification, we have five categories:

1) Experiment at atmospheric pressure. In this experiments, the range of temperature can vary from near-solidus ($650-1100^{\circ}\text{C}$) to low temperature. This category investigates the genesis of volcanic rock formed near at Earth's surface where the magma or lava has rapid cooling and volatiles are rapidly lost. Using quenching method, we determinate liquidus and subliquidus relations.

2) Experiments at moderate pressures and (up to 1 GPa). This group collected all experiments that investigate the genesis of plutonic rock and metamorphic rocks of low grade. These experiments permit us to understand the process of crystallization and differentiation of magmas, formation of migmatites, fluid interaction in metamorphic process, etc. . .

3) Experiments under high-pressures (HP) (over 1 GPa). These experiments reproduce the processes that occur at conditions of subduction zone, in the lithospheric and in the upper part of asthenospheric mantle. In these category of experiments the temperature conditions are highly variable and are related to the geological environment or process that has to be investigated. The studied process are the genesis of basalt melts, the formation of high and ultra-high pressure minerals (*HP-UHP*) and it investigated using natural or synthetic starting material that are pertinent at geological

conditions encountered.

4) Experiments under ultrahigh-pressures(UHP). As reported by Dobrzhinetskaya et al. (2013), this category uses: multianvil apparatus and diamond anvil cell (DAC) that allow us to test the behavior of minerals at the extreme conditions (e.g. mantle transition zone). The multianvil apparatus permits us to study the thermodynamic stability of UHP minerals, their phase transformations, and reproduction of melting processes of rocks. The multianvil can reach up to 25 GPa (700 km depth) and temperature ranging 1800-2000 °C. DAC can be used to extend our knowledge of mineral behavior from lower mantle to the mantle-outer core boundary. Both apparatuses, multianvil and DAC, allow us to measure the experimental during high-pressure and high-temperature experiment (e.g. X-ray diffraction synchrotron).

5)Miscellaneous experiments. The last category performs experiments implicating the physical proprieties of rock and minerals, such as, compressibilities, solubilities of volatiles in liquids, formation of ores, ecc. . .

In this thesis all experiments of host-inclusion systems are synthetized at conditions of high pressure over 2.5 GPa and high temperature ranging 775 °C to 1300 °C using piston cylinder end loaded of Milan University (Italy) and Syracuse University (NY-United States).

4.1 Piston cylinder apparatus

The piston-cylinder press is an apparatus developed by Pearson (1888), then Bridgman (1926) improved the original project and Boyd and England (1960a) adapted this instrument to problems of Earth sciences. Piston cylinder apparatus belongs of the solid media device group. It used in experimental petrology to reproduce pressure and temperature conditions of the Earth's

crust and/or mantle. We distinguish two type of piston cylinder: non end-loaded or single stage and end loaded. Two types differ in the fact that in the first type the pressure ram is applied to the smaller piston that acting on the sample. In the second type there is an additional hydraulic pump that produces an additional vertical load on the vessel. The piston cylinder end-loaded reach pressures higher than single stage because the shear resistance increases from additional vertical load on the vessel. The main components of piston-cylinder apparatus are: a) hydraulic pump that is the pressure generating system; b) the "bomb" that is a steel matrix containing a tungsten carbide core; c) The end-load ram and the so-called bridge (upper part), under which the piston ram is hidden; d) the pressure assembly components are inserted in the hole at the centre of assembly. Water cooling prevent thermal expansion of steel supporting and it circulates following a course around the vessel. The operating pressures is dependent by material used for the construction and by type of piston cylinder. In the piston cylinder single stage the pressure is applied by hydraulic ram only on the sample placed in the vessel and can be reached an operating pressure of 2.0 GPa. This value corresponds at transverse rupture strength of tungsten carbide. Piston cylinder end-loaded (Fig. 4.1) permits us to reach higher operating pressure because to its inside there are two hydraulic rams: first pressurized the apparatus (end load) and second is applied on sample. The ram at the top pressurized the vessel, then the pressure vessel is clamped between two platens. The ram at top increase the maximum value of tungsten carbide core to supports the pressure. Second ram transmitted the pressure at the piston into the pressure vessel pressurizes the sample placed in the pressure vessel; the ram provides the necessary load. For example at the Laboratory of Experimental Petrology of the University of Milan (Italy), the maximum

pressures reached by piston cylinder end-loaded are about 4.0 GPa. During the experiments, the temperature in the piston cylinder end loaded is generated by electricity passing through a graphite furnace of cylindrical shape. the temperature on the sample is measured by thermocouples. The pressure cannot be measured directly, the determination of the pressure must consider the geometry of apparatus and must be corrected for the friction effects between assembly and pressure vessel.

The pressure gauge of piston cylinder measures nominal pressure that is described by following formula:

$$P_{\text{oil}} = P_{\text{ram}} \left(\frac{R_{\text{large}}}{R_{\text{small}}} \right)^2$$

P_{ram} is pressure of hydraulic pump and second term is amplification factor, where R_{large} is radius of the part of the piston on which the oil pressure acts and R_{small} is radius of the piston acting on the sample. Decreasing upward of the piston size implies an amplification of the applied force that related to the reduction of area. The difference between nominal pressure (that reported by pressure gauge) and real pressure acting on sample is caused by friction effects between cylinder and piston walls.

$$P_{\text{real}} = P_{\text{nom}} + F_{\text{corr}}$$

The friction effects (F_{corr}) depend by operating condition, geometry of apparatus, type of assembly, ecc. . . and if one of these conditions is changed, the nominal pressure have to be determined again.

In order to calculate the real pressure, we need to calibrate piston cylinder through known phase transitions or reactions, melting curves or measured water solubility in melts. An ideal reaction for calibrating pressure must be

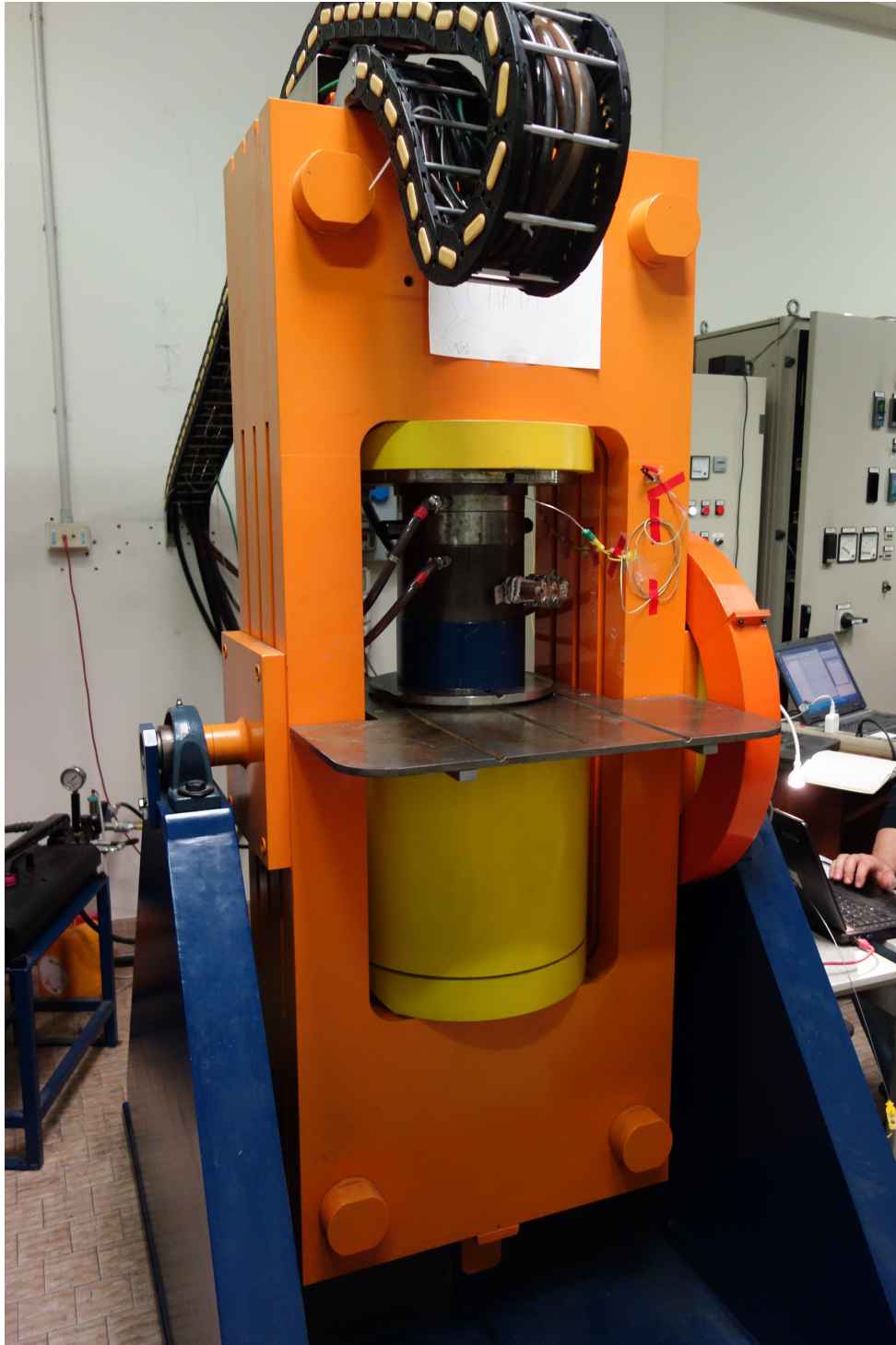


Figure 4.1: Rocking piston-cylinder at the Laboratory of Experimental Petrology of the University of Milan (Italy). The orange part can rotate of 180° during the experimental run.

insensitive to temperature. In this way the uncertainties on temperature do not contribute in the determination of the pressure. For example, it is often used the calibration based on quartz/coesite phase transition reported by Bose and Ganguly (1995).

4.2 Assembly

The choice of assembly components is fundamental to obtain a good result from experiments (Fig. 4.2). Assembly may have the capacity to transform the pressure from unidirectional, that is given by piston, to hydrostatic and it transmit at sample. The assembly must also heat the sample and for some experiments have to control oxygen fugacity. The pressure assemblies are concentric cylinders of refractory materials and it has to fit perfectly the sample chamber of piston cylinder. The capsule is placed at the center of the assembly. The capsule is accommodated in pressure transmitting cylinder (e.g. MgO, boron nitride) and it must be electrically insulating and must transmit the pressure in hydrostatic conditions. The graphite cylinder heats the experiments. The graphite furnace has a constant thickness or tapered design. The difference is that in first case the temperature is almost homogeneous along all cylinder, in the second case at the end of capsule will be more heater than in the center. The graphite furnace is insulated from external cylinder by the glass (pyrex) or quartz sleeve. The material for external cylinder must have a low friction coefficient to reduce the difference between nominal pressure and real pressure (e.g. NaCl, talc). The nominal pressure is always greater than the pressure acting on the sample. At the base of pressure assembly is placed a disk of graphite allowing the passage of electricity to heat the graphite furnace. The entire assembly is inserted in-

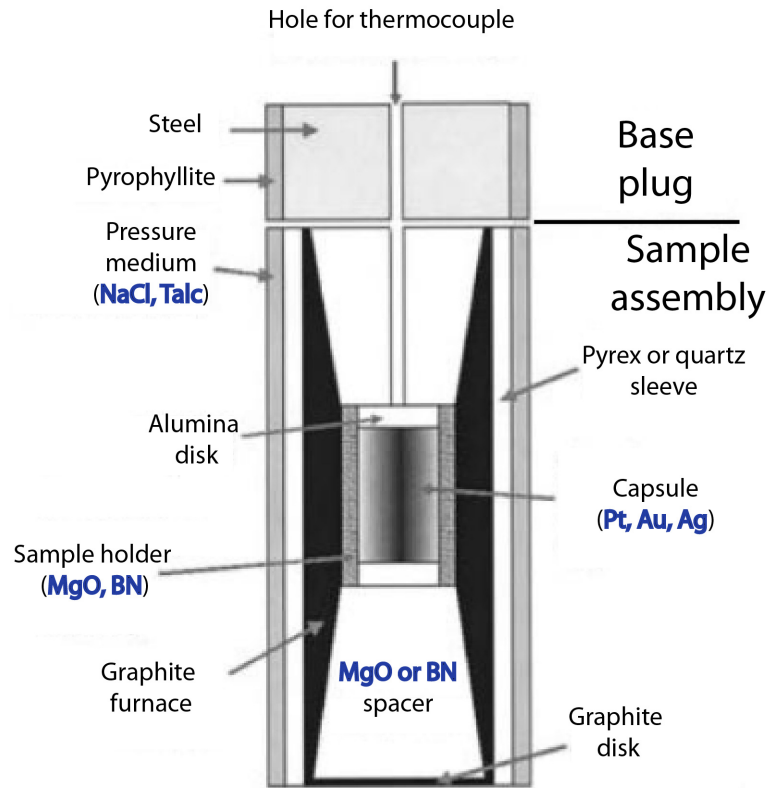


Figure 4.2: the sketch of piston-cylinder sample assembly made by Goffrey Bromiley 2007 and published by Miletich (2005a) and then modified for this thesis. The material reported in the figure are those used during my PhD

side the tungsten carbide core of the bomb. The temperature is measured by thermocouple and the measurement is close to sample capsule. Capsule and thermocouple are separated from corundum disk. The capsule is important part of experiments and it consists of noble metals (e.g. Au, Pt, AuPd). The choice of capsule and the assembly are in function of temperature, pressure and oxidation conditions.

Part II

Solid-State synthesis

Chapter 5

Introduction to solid-state synthesis

Aim of this study consists to synthesize an elastically isotropic host-inclusion pair at known P-T conditions from solid-state process by means of piston cylinder apparatus. Inclusions fully embedded in the host should show a residual pressure (e.g. Rosenfeld and Chase, 1961). On the samples recovered from high P-T experiments, the inclusion pressure can be determined using Raman spectroscopy or X-ray diffraction combined with knowledge of the elastic behavior of the inclusion mineral (Murri et al., 2018; Mazzucchelli et al., 2019; Angel et al., 2014b). Thus the entrapment pressure can back calculate at the temperature of synthesis and then be compared to the known pressure of entrapment. Match between the two values will confirm the reliability of the calculation of entrapment P-T by means of elastic geobarometry. This method can be applied only on ideal inclusions that are perfectly incorporate in the monocrystalline host at least 3 times of their radius and without fracture around it (Campomenosi et al., 2018; Mazzucchelli et al., 2018; Mazzucchelli et al., 2019).

An possible approach to synthesize an monocrystalline host around the inclusion is the solid-state process (Ikesue and Aung, 2006). This synthesis is basically a sintering process that consists in the removal of the voids between particles in the starting material applying pressure and temperature so that particles can grow and bond with adjacent grains (Richerson, 2005). This process is a common method in metallurgy, ceramic and plastic for compacting and forming a solid material. The quality of the final result depends by several factors. The process is driven by heat and pressure but without to reach the melting point of material. Control of temperature is fundamental to sintering. From the scientific literature the temperature has to be about 80-90% of melting material. Another important parameter is pressure that two grain-boundary diffusion and volume diffusion rely heavily upon temperature, the size and distribution of particles of the material, the materials composition, and often the sintering environment to be controlled. The starting powder for sintering process can be crystalline or non-crystalline (gel or glass). This process can be converted also for our purpose. As already reported Ikesue and Aung (2006) that Nd:YAG single crystal can be fabricated through the sintering method. A good result of crystal growth from sintering can be obtained only there is a monocrystalline garnet rod such as nucleation point (Ikesue and Aung, 2006). Following this approach and modifying for our aim, we want to synthesis a host-inclusion pairs with isolated and quite large inclusion inside the host. This method would permits us to have good control of position and size of inclusions inside the crystal and we can choose which inclusion to use for applying the elastic method. An optimal size for an inclusion should be at least 30 μm . On these inclusions we can measure their strain state by means X-ray diffraction and Raman spectroscopy. Using multiple instruments, we can compare the accuracy and precision of the

measurements for both instruments.

5.1 Experimental methods

The solid state experiments have been performed using HT Gas Mixing furnace (YAG6 experiment) and piston cylinder end loaded apparatus for all other experiments.

We loaded a capsule with monocrystalline rods together with powder of the same material (Fig. 5.1). In the powder we inserted an other phase that should have been trapped during the host growth. At high P and T the powder will grow as a single crystal following the crystallographic orientation of the rod (e.g. in epitaxial conditions with respect to the rod surface). We used two different monocrystalline rods for solid-state experiments: yttrium aluminum garnet (YAG) and natural pyrope. For YAG we had already the correct size of cylinder ($\phi=2.8$ mm) to insert in the Au or Pt capsule ($\phi=3$ mm). Concerning pyrope we extracted cylinder from natural crystal using a drill. The diameters of cylinders were of two sizes 1.8 and 2.7 mm. From cylinder we obtained the rod about 1mm thick using a diamond circular saw. In addition, the rod surface where the epitaxial growth occurs has to be mirror polished (up to 1 μm). The powder for both hosts has been produced by grinding YAG rod and natural pyrope (Fig. 5.2). Powders have to be a maximum size of 200 μm .

The other phases mixed in the powder are:

- For YAG experiments: Ruby, Si metallic, Ti metallic, diamond;
- For natural pyrope experiments: diamond, amorphous SiO_2 , synthetic cristobalite, natural quartz.

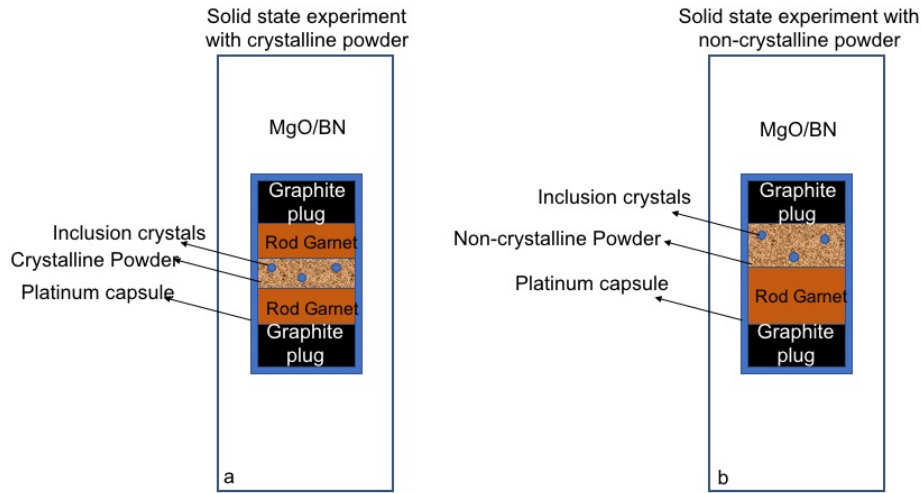


Figure 5.1: Sketch of starting material for solid-state experiments. (a) Inside capsule we inserted two monocrystalline rods and between them we inserted the powder of the same material of rod. The inclusions are placed in the crystalline powder. Two graphite plugs are inserted at top and bottom of capsule. (b) In the capsule there are two graphite plugs and one rod of garnet, over the rod there is the non-crystalline powder with the same composition of rod and into powder there are crystals of other minerals.

Cristobalite have been obtained by SiO_2 thorough heat treatment, the process will be explained in paragraph 5.3.2.

Table 5.3 describe all experimental details on YAG synthesis, all experiments synthetized to 3 GPa excluding YAG6 (at room P). All YAG experiments show 2 rod of Nd:YAG with powder of the same material.

Tables 5.4 and 5.6 describe all experimental details on natural pyrope synthesis, all experimental runs were at 3 GPa. For synthesis with diamond mineral phase the runs temperature was at 1300 °C. In the experiments with SiO_2 the temperature runs have been limited at 1200 °C and 1150° C to avoid a transformation in the cristobalite.

The choice of assembly and capsule was dependent by temperature and pressure conditions. The composition of the assembly is salt-pyrex with

graphite furnace for experiment under 1150 °C while over that temperature the salt-pyrex are replaced with talc-quartz assembly. The talc-quartz assembly is highly resistant to the high temperature, while the salt-pyrex melts. The capsules are accommodated in MgO or boron nitrate (BN) rods, the boron nitride distribute more homogenous the stress to high temperature (Tingle, 1988). BN rods and powder, both fired for 24 hours at 1100 °C before the experimental run. Corundum disk placed at the top of the MgO or BN rod to avoid contact between capsule and thermocouple, which could lead to the piercing of the capsule. For experiments we used gold or platinum capsule. The melting point of platinum is higher than gold (respectively 1768 °C and 1064 °C at room pressure), thus Pt is used to high temperature. In these experiments is important to avoid fracturing of the host because in that case the elastic geobarometry cannot be applied. Then YAG7 to prevent cracking during the quenching of experiment, Tingle (1988) proposed a protocol that use two practical arrangements: First, we placed at the top and the bottom of the capsule two graphite plugs because they accommodate the stress release. Second we performed a linear and slow ramp up and down for temperature and pressure that should avoid fracturing of the crystal Tingle (1988). Samples were first pressurized to $P = 0.25$ GPa, heated to $T = 800$ °C and then pressurized and heated simultaneously up to 1 GPa and 1000 °C. At this temperature, the sample must be pressurized up to 3 GPa and in the final step we only heated sample keeping constant pressure (see Fig. 5.3). Temperature rate was 50 °C/minute until reaching the final value. From run conditions to room P and T the experiments were depressurized approximately at a rate of about 80/100 MPa/min with a temperature cooling ramp in 2 steps from 1300/1200 °C to 1000 (to 2.5 GPa) and from 1000 to 200 °C (simultaneously to pressure) and final temperature

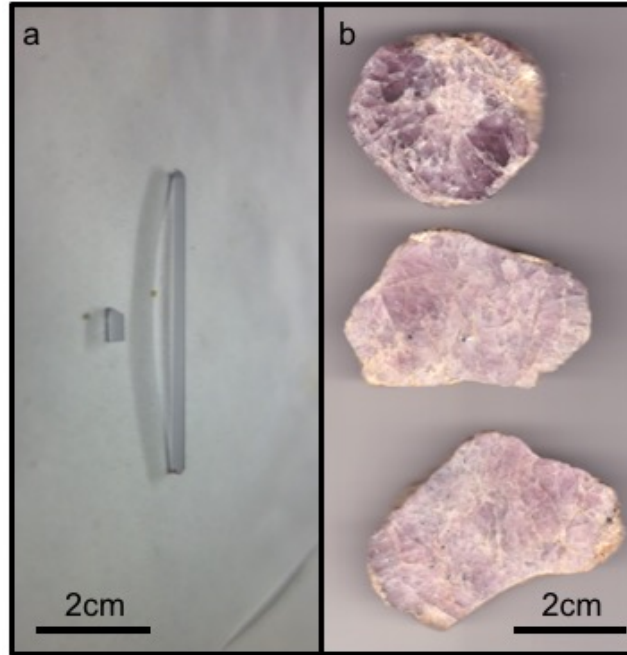


Figure 5.2: Starting material used as host for solid state experiments. (a) Nd:YAG Rod without impurity of 3 cm of diameter. (b) Natural pyrope ($\text{Mg}_2\text{Al}_2\text{Si}_3\text{O}_{12}$ 95%) from Dora Maira (Italy).

step from 200 to room 25 °C (to room P , see Fig. 5.3). For all cooling ramps the temperature rate was less than 50 °C/minute. From Py7, in contrast with the previous experiments where we followed a linear and slow ramp up and down, these new runs have been fast cooled down and decompressed. Temperature was measured with K-type thermocouple sited within 0.6 mm of the capsule for experiment under 1300 °C while for experiment to 1300 °C we used the thermocouple S-type. Both thermocouples are considered accurate for ranging about ± 5 °C. Experiments were performed for range run time from 24 to 144 hours (see Tables 5.3, 5.4 and 5.6). After quenching the run the capsules were mounted in epoxy and polished.

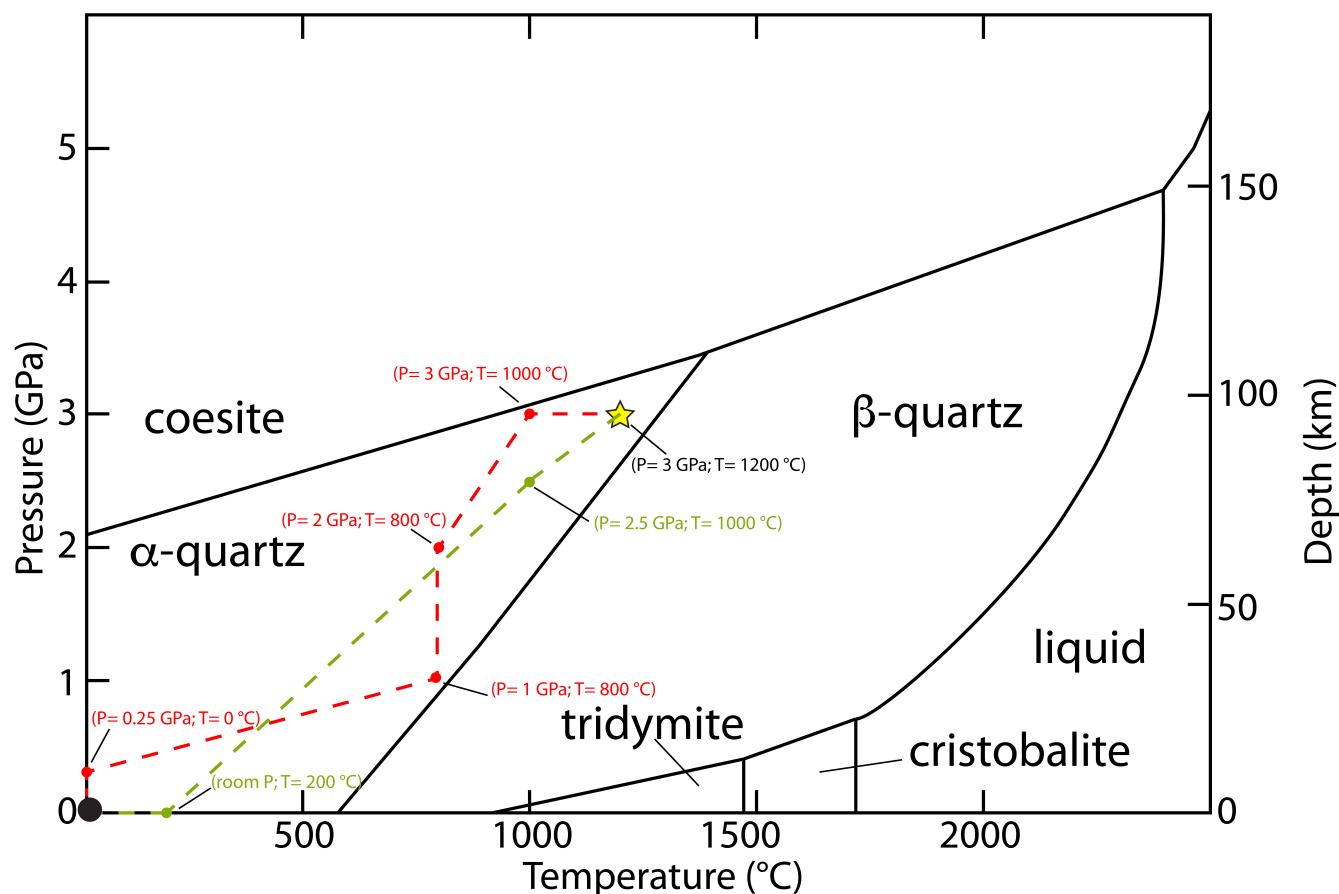


Figure 5.3: show P-T phase diagram of silica published by Sanloup et al. (2005). On the diagram are reported the ramp up and down for all experiments with SiO₂. The ramps for this experiments have two aims: a) to remain in the quartz stability field for the whole experiment; b) to avoid the fracture in the host crystal produced during depressurization and cooling. The black circle shows starting point and the final point of experiments and the yellow star are the P-T experimental conditions of Py4, Py5, Py6, Py7, Py10 and Py11 experiments. Dashed red path shows the ramp up and red dots are the intermediate steps to reach experimental conditions. Dashed green path shows the ramp down and green dots are intermediate steps to reach the final conditions.

5.1.1 Analytical techniques

All samples were also inspected using back scattered electron (BSE) imaging and characterized by electron microprobe analyses and maps using a JEOL JXA 8200 Superprobe equipped with five wavelength-dispersive (WDS) spectrometers and an energy dispersive (EDS) spectrometer (accelerating potential 15 kV, beam current 15 nA), at the Department of Earth Sciences, University of Milan. We conducted electron backscatter diffraction (EBSD) analysis on Py6 and Py7 samples using a Camscan MX2500 SEM equipped with a LaB₆ filament at the University of Padova. In some cases the quality of sintering process have been analyzed by single-crystal X-ray diffraction measurements using the 8-position centering method proposed by Angel and Finger (2011) using a newly developed Huber 4-circle Eulerian cradle diffractometer equipped with point detector and microfocus source (120 μm spot size). The graphite/diamond inclusions have been analyzed using parallel-polarized Raman spectra in backscattering geometry with a Horiba Jobin-Yvon T64000 triple-monochromator spectrometer (spectral resolution of 2 cm^{-1} , instrumental accuracy in peak positions of 0.52 cm^{-1} $1\text{ }\mu\text{m}$ spot size) with a 532 nm green laser. The initial aim of Micro-Raman spectroscopy was to analyze the Raman shift of inclusion to calculate the residual, unfortunately there were not ideal inclusions to analyzed.

5.1.2 Gel and glass preparation

As better explained in paragraphs 5.3.2 and 5.4 the sintering process improves significantly at higher temperature, therefore after EBSD analysis we observed that crystalline powder is few reactive to grow single crystal. Thus we replaced the crystalline powder with non-crystalline powders (gels and

glasses) of pyrope because it should be more reactive. The Py10 and Py11 experiments have been performed at 3 GPa and 1200°C

For the gel preparation we followed the approach by Biggar and O'hara (1969). Employing nitric solutions of magnesium and aluminum and Tetraethyl orthosilicate (TEOS) for Si (see Table 5.1). The gelling process is very long because it needs of several steps. First step is added the weighted solutions in a becker with magnetic stirrer. Magnesium solution, aluminum solution and TEOS added in this order in the becker. At the solutions have to be added ethanol to obtain a homogenous mixture. We have to remember that TEOS need a part of ethanol. The mixture is blended using magnetic stiffer and increasing the temperature. The addition of ammonia to mixture is necessary to obtain the co-precipitation. The ammonia has to be added until to pH value about 8 or 9. The gel must be at room temperature for 24 hours and then is put in the furnace about 100 °C for 3 or 4 days to remove the water. The temperature in the furnace must increase of 30 °C each 2 hours up to 250 °C hours to remove nitrate and hydroxides. Then the gel must be grinded using pestle and mortar. Last step is burn it to 1000 °C to remove nitrates using Bunsen burner and grinded again. The glass of pyrope is prepared starting stoichiometric mixture of oxides (MgO, Al₂O₃ and SiO₂ in Table 5.2). Afterward the mix of oxides is melted over liquidus temperature of pyrope (1650 °C) to obtain a homogeneous glass (Irfune and Ohtani, 1986; Zhang and Herzberg, 1994).

5.2 Experiments with crystalline powder - YAG

For the first solid state experiments of host inclusions we used YAG (Y₃Al₅O₁₂) a synthetic garnet of yttrium and aluminum. We choose YAG as host because

Table 5.1: Composition of oxides mixture used to produce gels of pyrope.

Oxides for pyrope	Wt%	mL to be used	resulting grams
MgO	30.00	14.9	0.300
Al ₂ O ₃	25.00	12.3	0.251
g to be used			
SiO ₂	45.00	1.793	0.450
Total	100.00		1.001

Table 5.2: Composition of oxides mixture used to produce glass of pyrope. Weight measured to produce 0.5g of glass.

Oxides for pyrope	oxides theoretical weight (g)	oxides weighed (g)	difference
Al ₂ O ₃	0.1265	0.1263	0.0001
MgO	0.1500	0.1497	0.0003
SiO ₂	0.2236	0.2234	0.0002
Mg ₃ Al ₂ Si ₃ O ₁₂	0.5000	0.4994	0.0006

it has similar elastic proprieties of natural garnet (e.g. S. Rezende, 2014) but the growth rate of YAG is faster than natural garnet. As reported Ikesue and Aung (2006) Nd:YAG have growth rate approximately of 0.2 mm/h to T 1970 °C with Czochralski method. Ikesue and Aung (2006) showed in their study that crystal growth rate was mm/h order at the temperature > 1700 °C in few days using sintering method.

Table 5.3: Summary of all solid-state experiments with YAG as host and crystalline powder. In the Table are reported all details experiments.

Experiment Name	Assembly	Capsule			Starting materials			Experimental conditions			Ramps	
		Material	diameter	graphite plugs	YAG Rod	Powder	Inclusions	Temperature (°C)	Pressure (GPa)	Time (hours)	Up	Down
YAG3	salt pyrex	gold	Ø=3 cm	no	2	crystalline yag	ruby	1000	3	144	-	quench
YAG4		gold	Ø=3 cm	no	2	crystalline yag	ruby	1200 growth 800 elastic resetting	3	120	-	quench
YAG5		gold	Ø=3 cm	no	2	crystalline yag	ruby	1300 growth 800 elastic resetting	3	96	-	quench
YAG6	-	platinum	Ø=3 cm	no	2	crystalline yag	-	1700	room P	48	-	quench
YAG7	salt pyrex	platinum	Ø=3 cm	no	2	crystalline yag	Si metallic	1300	3	30	-	quench
YAG8		platinum	Ø=3 cm	yes	2	crystalline yag	Ti metallic	1300	3	24	YAG7	YAG7
YAG9		platinum	Ø=3 cm	yes	2	crystalline yag	diamonds	1300	3	24	YAG7	YAG7
YAG10		platinum	Ø=3 cm	yes	2	crystalline yag	diamonds	1300	3	24	YAG7	YAG7
YAG11		platinum	Ø=3 cm	yes	2	crystalline yag	diamonds	1300	3	24	YAG7	YAG7

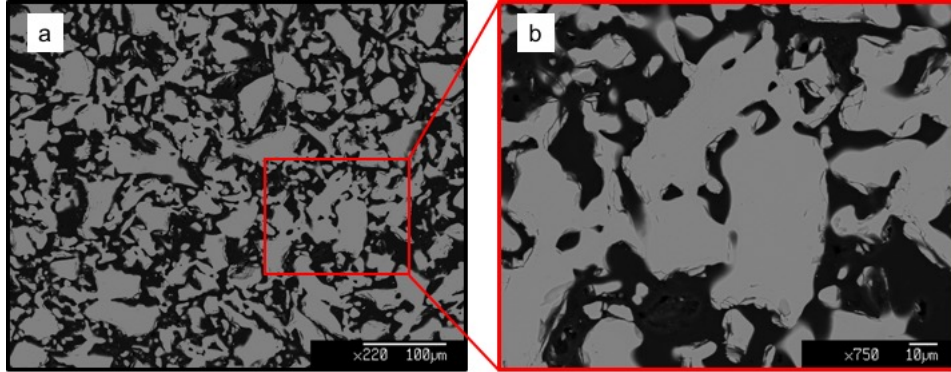


Figure 5.4: reported experiments YAG6 that performed at 1700 °C and room P using gas mixing. (a) Image in BSE that show the results of sintering degree. (b) Details of sintering degree YAG6 show a neck formation between grains, but the porosity is not decreased because the sintering is occurred without pressure.

5.2.1 YAG Sintering experiments at room P and $T=1700^{\circ}\text{C}$

YAG6 was performed without other phases (Fig. 5.4) at close melting conditions (1700 °C) and room pressure using gas mixing. We used these experimental conditions to understand the role of temperature and pressure during the sintering of the YAG. As shown in Fig. 5.4b, we observed that the bonding is occurred where the grains were in contact, but porosity is not decreased. Then the pressure is fundamental to obtain sintering of high quality.

5.2.2 YAG experiment with ruby at $P= 3 \text{ GPa}$ and $T=1300^{\circ}\text{C}$

The first experiments are YAG3, YAG4 and YAG5 (see Table 5.4). The ruby(Al_2O_3) was inserted in the YAG powder, we used this mineral phase to avoid the reaction between host and inclusions during the sintering process. The size of rubies were around 100-200 μm . YAG3 performed at 3 GPa and

1000 °C. For YAG4 and YAG5 experiments we increased the temperature of sintering. In YAG4 and YAG5 we synthesized at 1200 °C and 1300 °C, before the quenching experiments we held them at 800 °C to re-equilibrate (for 3 days) the inclusion at eclogitic facies. The gold capsules were dissolved using aqua regia because it is a non-invasive method, nevertheless this precaution, all final YAG experiments were highly fractured. The final results were a lot of YAG disk with thickness less than 0.3 mm. The fracturing has not been reduced from increased temperature. The YAG disk has been analyzed using X-ray diffraction, but we did not find evidence of the presence of ruby inclusions.

5.2.3 YAG experiment with Si and Ti metallic at $P = 3$ GPa and T ranging from 1000 to 1300°C

Previous experiments we indicated that YAG has a lot of fracture and low degree of sintering. From YAG7 we performed experiments at 1300 °C and 3 GPa. For this temperature we changed the capsule from Au to Pt, because Pt has a higher melting point. For these experiments we changed the setup because we inserted two plugs of graphite inside the capsule at top and at bottom to prevent the cracks (Tingle, 1988). From these experiments we have pressurized and depressurized following ramps reported in the paragraph 5.1. We changed the inclusion because ruby is a good material to avoid reaction with YAG (Nagira et al., 2012), but it is not good inclusions to apply the elastic geobarometry method. For these experiments we choose Si and Ti metallic as inclusion because they have a bulk modulus lower than YAG. In experiments YAG 7 we inserted Si metallic in the YAG powder. From chemical analysis, we observed that Si and Pt reacted and formed metal alloy in accordance with Yang et al. (2004). In Fig. 5.5b at top of Si inclusions we can observe

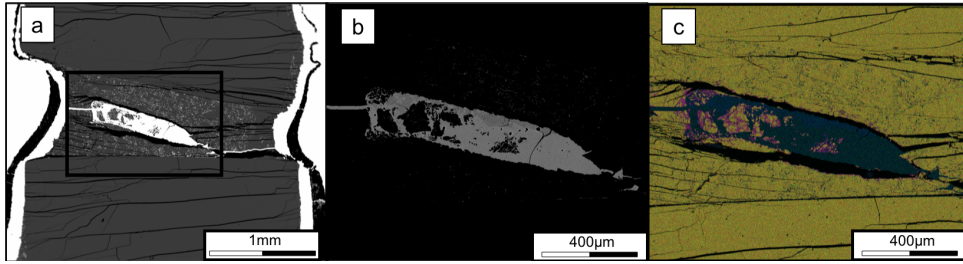


Figure 5.5: (a) reported experiments YAG7 that performed at 1300 °C and 3 GPa using piston cylinder apparatus. (b) BSE image shows heterogeneity composition of metallic Si inclusions. Inclusion is partially melted and have a reactivity rim in contact with YAG. (c) The combined Y-Al-Si chemical element maps in RGB show the different inclusion phases with YAG in Yellow, Si in blue and Alloy Y-Si in violet.

a partial melting of Si. As shown Fig. 5.5c Si metallic reacted also with YAG forming new phases. For YAG8 we changed the inclusion, we putted in the powder the Ti metallic. Also, in these experiments we observed that the inclusion reacted with capsule, this process is well observable using optical microscope. The Pt capsule shows a bluish color.

5.2.4 YAG experiment with diamond at $P = 3 \text{ GPa}$ and $T = 1300 \text{ °C}$

From YAG9 we inserted synthetic diamond as inclusions because it is well-known as such few reactive with other minerals. We used synthetic diamond with rounded and prismatic shapes. We insert this mineral phase because diamond is considered typically inert material. For synthesis YAG9 and YAG10 the results are unknown. There were several problems with setting of temperature parameter on the piston cylinder apparatus. In both experiments we passed the melting point of the platinum capsule and then the final products were unusable. For experiment YAG11, the results show that YAG reacted with diamond inclusions. The new phases consist of corundum and

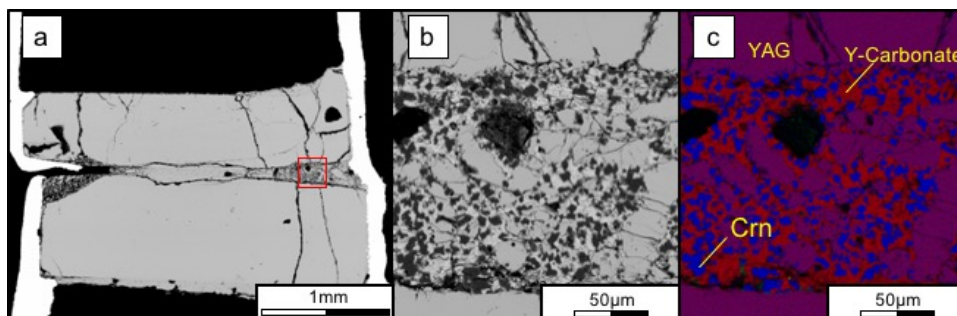


Figure 5.6: (a) reported experiments YAG11 that performed at 1300 °C and 3 GPa using piston cylinder apparatus. (b) BSE image shows heterogeneity growth of crystalline powder. Inclusions are totally or partially dissolute and formed several new mineral phases. (c) The combined Y-Mg-Al chemical element maps in RGB show the different inclusion phases with YAG in Yellow, Si in blue and Alloy Y-Si in violet.

anhydrous yttrium carbonate (Fig. 5.6). There are only few inclusions that maintained the starting shape. From reported data the sintering process has been suppressed by high reactivity of YAG. Therefore the process of sintering has been constrained well during this set of experiments from YAG3 and to YAG1. The YAG as a host turned out to be a major problem as host because of its extremely high reactivity with the inclusion phases and with the assembly materials. So, we choose to change the host.

5.3 Experiments with crystalline powder - pyrope

At this point as consequence of YAG reactivity, we delineate a new strategy for host. The change of host, from YAG to Dora Maira's Pyrope (natural garnet). The Dora Maira's garnet megablasts (Fig. 5.2b) consist of pyrope (90-98 mol.%) and their composition are relative homogeneous in the all crystals (e.g. Chopin, 1984; Simon et al., 1997; Compagnoni and Hirajima, 2001). This new crystalline host improved significantly the results (see Table 5.4). We performed 9 experiments using the same setting of previous experi-

ments. All rods used as center of nucleation have been drilled from 2 crystal that are reported in Fig. 5.2b. We used drill of the Department of Earth and Environmental Sciences at Milano Bicocca University. We performed some cylinders from natural garnet of two diameters 1.8 and 2.7 cm. During these experiments we have understood also that the sintering process improved with new host. We performed the experiments to several time condition to understand the relevance of time on the growth of grains and on reactivity of natural materials. The experiments synthetized from 24 to 138 hours. The types of inclusions that we tested in these experiments was diamond and SiO_2 . We insert several SiO_2 phases that are reported in paragraph 5.3.2.

Table 5.4: Summary of all solid-state experiments with pyrope as host and crystalline powder. In the Table are reported all details experiments.

		Capsule		Starting materials			Experimental conditions				Ramps		
Experiment	Name	Assembly	Material	diameter	graphite plugs	YAG Rod	Powder	Inclusions	Temperature (°C)	Pressure (GPa)	Time (hours)	Up	Down
Py1	salt pyrex	Pt	Ø=2 cm	yes	2		crystalline natural pyrope	diamonds	1300	3	24	YAG7	quench
Py2		Pt	Ø=2 cm	yes	2		crystalline natural pyrope	diamonds	1300	3	24	YAG7	YAG7
Py3		Pt	Ø=2 cm	yes	2		crystalline natural pyrope	diamonds	1300	3	24	YAG7	YAG7
Py4	talc qz	Pt	Ø=3 cm	yes	1		crystalline natural pyrope	silica gels	1200	3	90	YAG7	YAG7
Py5		Pt	Ø=3 cm	yes	2		crystalline natural pyrope	silica gels	1200	3	44	YAG7	YAG7
Py6		Pt	Ø=3 cm	yes	1		crystalline natural pyrope	Silica gels dehyd	1200	3	117	YAG7	YAG7
Py7		Pt	Ø=3 cm	yes	1		crystalline natural pyrope	Silica gels dehyd	1200	3	138	YAG7	quench
Py8		salt pyrex	Pt	Ø=3 cm	yes	1		crystalline natural pyrope	natural quartz	1150	3	67	YAG7
Py9	Pt		Ø=3 cm	yes	1		crystalline natural pyrope	cristobalite	1150	3	46	YAG7	quench

5.3.1 Diamonds in pyrope at $P = 3$ GPa and $T = 1300$ °C

In the first experiments with pyrope we used diamond inclusions. We performed Py1, Py2, Py3 with synthetic diamonds. Inclusions have a size about 30 μm with cubic or sub-rounded shape. The time of sintering for these experiments was of 24 hours. From BSE images on experiment Py1, we observed that the host show a partial melting. As shown in Fig. 5.7a and 5.7b the melt is concentrated along all the pyrope rods, around to grains of powder. The partial melting generated a reaction rim along the rod garnet. In the starting pyrope we have about 4wt.% of almandine therefore the rim composition consists of a pyrope pure ($>99\%$). This indicate that the reaction rim removed all iron through diffusion process. In grains of powder we occurred the same process of diffusion (see Fig. 5.7c and d), but the migration rates are higher than in the rod. As reported in Table 5.5, the iron decrease from core to rim of grains. The rods of Py1 included the hydrous minerals (e.g. phengite) that decreased the melting point of pyrope. In new experiments the natural rods have been analyzed at the optical microscope to choose those without inclusions, but in some case the inclusions were not detectable.

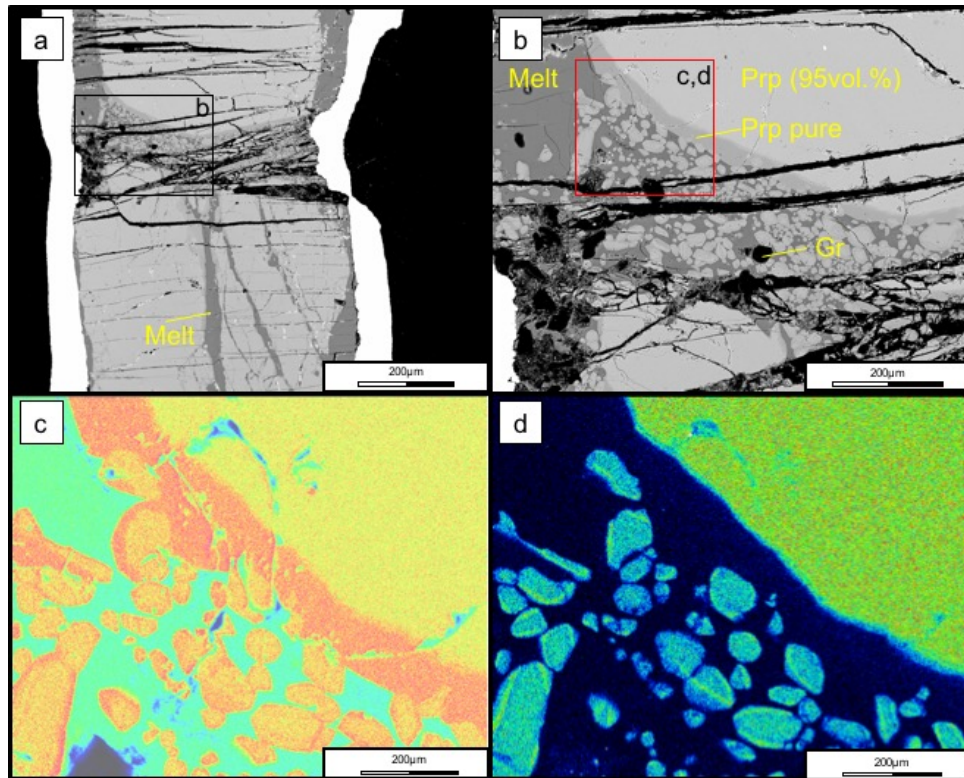


Figure 5.7: shows Py1 experiment that performed at 1300 °C and 3 GPa for 24 hours. (a) In BSE image, we observe partial melting of host. (b) BSE image is a detail of Py1 that shows a reaction rim of along the host and the presence of partial melting. The sintering between rod and powder did not occur, the grains are surround of melt. (c,d) are chemical maps, respectively of Mg and Fe. Warm colors indicate high concentrations and cold colors indicate low concentrations of the respective elements. These maps show a chemical zoning inside rod and grains of pyrope. Reaction rims of garnet rod and grains consist of pure pyrope (>99%).

Table 5.5: Representative chemical analysis made on the Py1, after sintering experiments. The host crystal show processes of partial melting and chemical diffusion. the chemical data obtained using by EMPA analysis.

phase	rod Prp starting	rod Prp starting	rod Prp starting	Rod reacted rim	melt	melt	powder single crystal (inner core)	powder single crystal (external core)	powder single crystal (internal rim)	powder single crystal (external rim)
point analysis	PY1-1	PY1-2	PY1-3	PY1-4	PY1-5	PY1-6	PY1-7	PY1-8	PY1-9	PY1-10
N. analysys	1	2	3	4	5	6	7	8	9	10
Na ₂ O	0.1086	0.0952	0.0913	0	0.0632	0.0866	0.0565	0.0162	0.0222	0
MgO	25.62	25.71	25.72	29.5	18.17	18.28	27.28	27.95	28.58	30
SiO ₂	43.24	43.49	43.4	44.36	37.21	37.35	43.35	40.82	43.24	43.91
FeO	4.18	4.3	4.26	0.1683	0.0764	0.0015	2.59	2.36	1.9	0.1025
CaO	0.9091	0.8999	0.9365	0.0767	0.7078	0.6735	0.6183	0.1034	0.1187	0.0868
Al ₂ O ₃	24.71	24.84	24.8	25.21	20.98	21.38	25.43	25.38	25.48	25.91
Total	98.7758	99.3973	99.2078	99.315	77.2474	77.7716	99.3248	96.7134	99.3898	100.0093

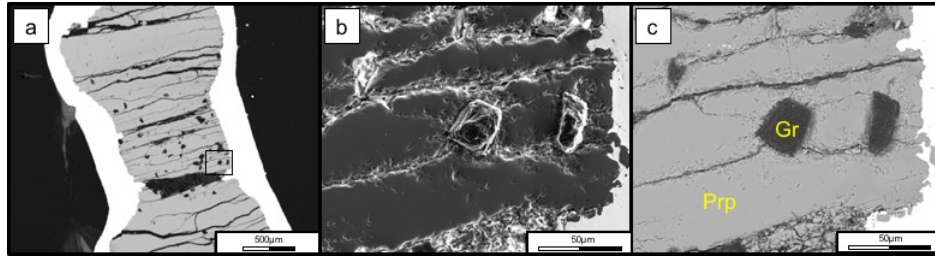


Figure 5.8: show experiment Py2 that performed at 1300 °C and 3 GPa for 24 hours. (a) BSE image shows that inclusions trapped in garnet. (b) the detail image of Py2 in SE shows the morphology of cubic or sub-rounded graphite inclusions. The radial fractures are typically around of inclusions. (c) BSE image is made on the same zone of (b) and it shows the homogenous composition of garnet (without reaction rim).

In Py2 and Py3 we do not evidence any process of partial melting (for example Py2 in Fig. 5.8a). In both experiments the inclusions seem entrapped in a host. On these inclusions combining several techniques we identify their features. From optical analysis, inclusions show black color and opaque that are not typically features of diamonds, but they maintained the original shape of synthetic diamonds crystals. And we found inclusions that are fully entrapped in garnet (Fig. 5.8c and 5.9a).

The inclusions show radial fractures, which are propagate the corners of the inclusion crystals and can be released partially pressure. So, we measured the Raman spectra of cubic inclusions to investigate if they show a partial residual pressure. But the Raman spectra were not those of diamonds but of order graphites, such as reported in Fig. 5.9b. And in both experiments all diamond crystals were subject a total conversion to graphite. SE images (Fig. 5.8b) of cuboidal graphite show small hills and depressions. Korsakov et al. (2019) demonstrated that the graphite cuboids represent polycrystalline aggregates composed either of numerous smaller graphite cuboids.

For our purpose, diamond inclusions show an extremely fast reaction rate

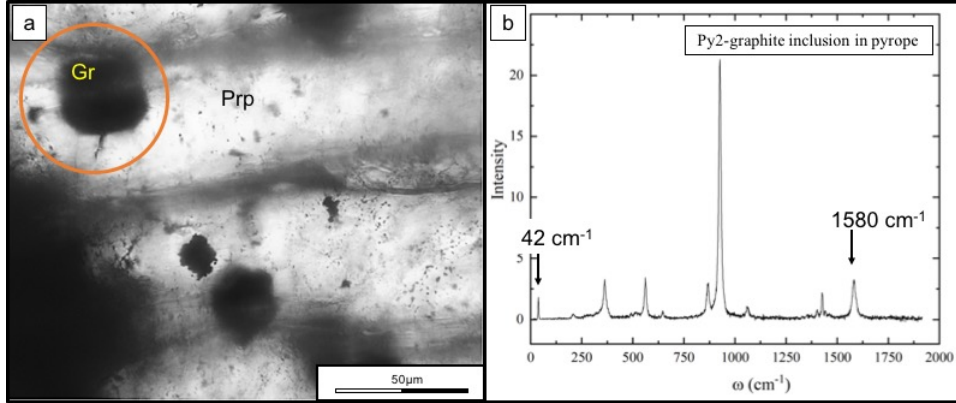


Figure 5.9: in optical image (a) we observed a cubic graphite inclusion included in pyrope. The Raman spectra (b) is concerned to inclusion in orange circle of image (a). In Raman spectrum we reported the peak position of order graphite. The Raman peak position of garnet host are from 208 cm^{-1} to 1062 cm^{-1} . At range from 1400 to 1500 cm^{-1} there are Raman peak position of epoxy resin.

at $P = 3\text{ GPa}$ and $T = 1300\text{ }^{\circ}\text{C}$, indeed all diamond converted to graphite, so they are not good inclusion. As a consequence, we changed the type of inclusions.

5.3.2 SiO_2 in pyrope at $P = 3\text{ GPa}$ and T ranging from 1150 to $1200\text{ }^{\circ}\text{C}$

We choose to use sphere of silica gel (SiO_2). In this series of experiments from Py4 to Py9 we decide to develop for couple of experiments, for each pair we changed a single variable. For first couple of experiment, the only difference is that Py4 has a one rod and Py5 has two rods. In both experiments we inserted the sphere of silica gel. The sintering with one rod is always good and we can reduce the starting material to have more control on the natural inclusions. The inclusions from silica gel have totally or partially melted. In the following experiments we inserted only one mono-crystalline rod. In

the Py6 and Py7 we tried to use heterogeneous and homogeneous rods to understand how they influence sintering growth. In these experiments we inserted dehydrated SiO_2 sphere to understand if the presence of water can explain the total or almost total melt of inclusion in previous experiments. For dehydrating we heated SiO_2 until 200 °C for 2 hours. These experiments showed that when the rod surface contains second phase, such as Py6, sintering growth is suppressed; in order we obtained a single crystal in Py7 and a poly crystal in Py6. In Fig. 5.10a the experiments Py7 show also a diffusion from core to rim in grains of powder. In the chemical map of Fig. 5.10b we can observe the quartz inclusions that are entrapment in Pyrope powder. The inclusions showed an irregular shape because they are too soft. Inclusions are again surrounded by melt. We observed that in the experiments with dehydrated amorphous silica showed a very low or absent rate of partial melting of inclusions. Therefore we cannot insert amorphous sphere of SiO_2 because the reactivity is too high. For experiments Py8 and Py9 we decide to use crystalline SiO_2 , respectively natural quartz and synthetic cristobalite. Natural quartz inclusions obtained by grinding of piece quartz using pestle and mortars, the grains obtained had irregular shape and size about 30-60 μm . While the spherical inclusions are obtained from sphere of silica gel that previously they have been crystallized at high temperature to have a crystalline polymorph of SiO_2 (cristobalite). Both experiments do not show partial melting. For experiments Py8 the irregular inclusions of natural quartz show radial fracture starting from corner of crystals. While crystalline sphere (cristobalite) are not melted or fractured. During the experiments cristobalite is turned into quartz.

From EBSD results on experiment Py7 (see Fig. 5.10d) show that the c-axis of the powder are randomly oriented. The crystalline powder of pyrope

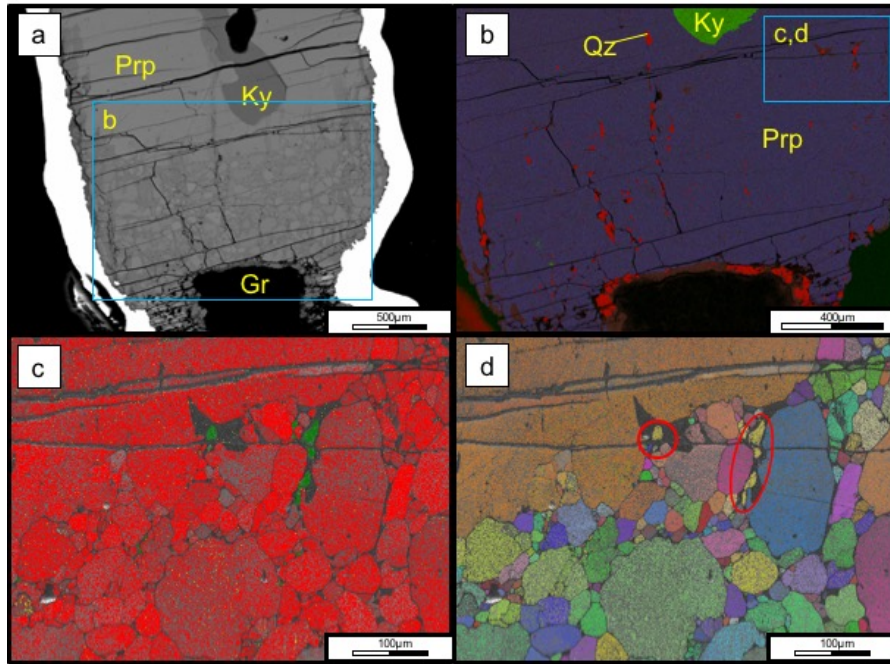


Figure 5.10: reported experiments Py7 that performed at 1200 °C and 3 GPa for 138 hours. (a) BSE Image show composition of rod that included a natural kyanite inclusion. Powder growth is reported in blue square. The blue square indicates the zone where it has been made the chemical maps (b). The combined Si-Al-Mg chemical element maps in RGB show the different inclusion phases with quartz in red, kyanite in blue and Pyrope in purple. EBSD mapping of the sintering experiment Py7 reported in images (c,d). EBSD mapping the positions of quartz included in garnet powder. (c) The orientations of the C-axis of the garnet rod (orange large crystal) and powder (multicolor small grains). In red circles are reported the orientation of quartz inclusions. The same color (yellow) indicate that all quartz inclusions have the same orientations.

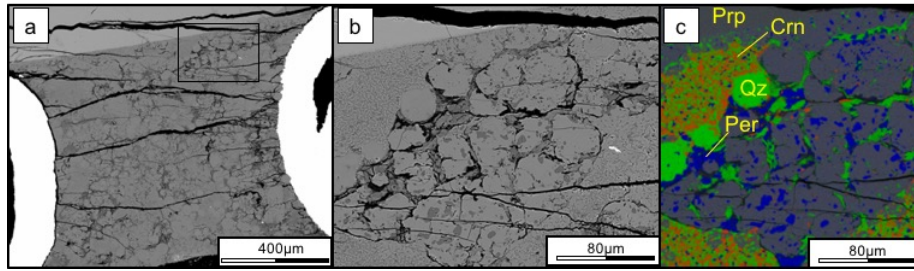


Figure 5.11: BSE image of Py10 (gel powder). (b) detail of synthesis results in BSE image, that show growth heterogeneity of gel powder. (c) The combined Al-Si-Mg chemical element maps in RGB show the different inclusion phases with corundum in red, quartz in green, periclase in blue and pyrope in grey

is not a good starting material to epitaxially grow as demonstrated by our EBSD results (Fig. 5.10c and d). The growth of crystalline powder as single crystal is too slow (>120 hours). The grains of powder did not grow during the experiments. So for this result we decide to develop this experiments with another approach that reported in the next paragraph.

5.4 Experiments with non-crystalline powder at $P = 3$ GPa and $T = 1200$ °C

From EBSD analysis on solid-state experiments with crystalline powder we have understood also that the sintering process improves significantly at higher temperature therefore the time to grow suitable sized grains is too long to have single crystals. At this point we replaced the crystalline powder with non-crystalline powders (gels and glasses) of pyrope (Table 5.6) because it is more reactive. For both experiments we had significantly improved the quality of the host producing larger single crystals as shown in Fig. 5.11 and 5.12. In these experiments the inclusions were cristobalites. In the experi-

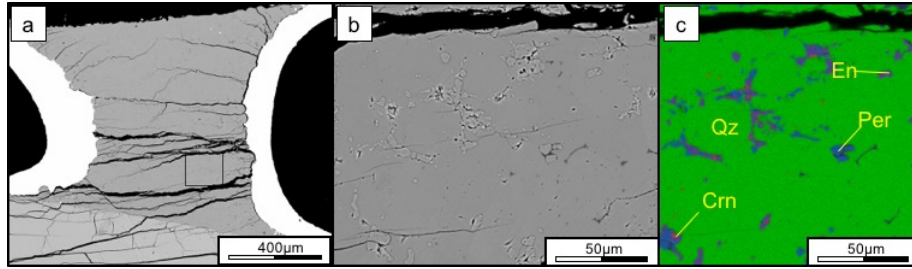


Figure 5.12: BSE image of Py11 (glass powder). (b) detail of synthesis results in BSE image, that show quite homogeneity growth of glass powder. (c) The combined Al-Si-Mg chemical element maps in RGB show the different inclusion phases with corundum in red, quartz in green, periclase in blue and enstatite in purple.

ment Py10 we used gels of pyrope as non-crystalline powder. As shown Fig. 5.11a and b, we obtained a host with few fractures and without partial melting. However, host grew heterogeneous and because we had an unexpected growth of four mineral phases: pyrope, corundum, quartz and periclase, as reported chemical map in Fig. 5.11c. We obtained a large part of pyrope as host with a lot of inclusions with irregular shape. While in the experiment Py11 we used the glass powder. In this experiment have been produced homogeneous large hosts with several small inclusion (Fig. 5.12a and b). As shown the Fig. 5.12c the problem here is that large host is a quartz crystal and inclusions consist of periclase, enstatite and corundum. In this case the nucleation started by crystalline inclusions (cristobalite).

Table 5.6: Summary of all solid-state experiments with pyrope as host and non-crystalline powder. In the Table are reported all details experiments.

Experiment Name	Assembly	Capsule			Starting materials			Experimental conditions			Ramps	
		Material	diameter	graphite plugs	YAG Rod	Powder	Inclusions	Temperature (°C)	Pressure (GPa)	Time (hours)	Up	Down
Py10	talc qz	Pt	Ø=2 cm	yes	1	gel of pyrope	crystobalite	1200	3	77	YAG7	quench
Py11		Pt	Ø=2 cm	yes	1	glass of pyrope	crystobalite	1200	3	70	YAG7	quench

Part III

Hydrothermal synthesis

Chapter 6

Assessment of the reliability of elastic geobarometry with quartz inclusions

This chapter has been adapted from a manuscript, recently submitted for publication to *Lithos*, with the title: Assessment of the reliability of elastic geobarometry with quartz inclusions, authored by M. Bonazzi, S. Tumati, J. Thomas, M. Alvaro2, R.J. Angel, M. Alvaro.

6.1 Abstract

Elastic geobarometry makes use of the contrast in elastic proprieties between host and inclusion crystals to determine the entrapment conditions of the inclusions from the residual stress and strain measured in the inclusion when its host is at ambient conditions. The theoretical basis has been developed extensively in the past few years, but an experimental validation of the method is still required. We synthesised quartz inclusions in pure almandine garnet

at eclogitic conditions $P=3.0$ GPa and $T=775$ °C; and at $P=2.5$ GPa and $T=800$ °C in a piston-cylinder press and measured the Raman spectra of isolated, fully-enclosed quartz inclusions in the recovered garnets. All fully-buried inclusions exhibit Raman peaks at higher frequencies and wavenumbers than those obtained from quartz crystals at ambient pressure. If these peak shifts are interpreted as a remnant pressures by use of hydrostatic calibrations of the Raman shifts of quartz with pressure, the remnant pressures show a large spread in values and lead to significant errors in back-calculated entrapment pressures, of up to 1.4 GPa for inclusions synthesised at 3.0 GPa. These results confirm that quartz inclusions trapped inside garnet are not subject to hydrostatic pressure.

We therefore used the phonon-mode Grüneisen tensors of quartz to calculate the full strain state of each inclusion, from which the full anisotropic stress state can be calculated by using the elastic properties of quartz. The mean residual remnant stress of the inclusions determined in this way show a much smaller spread in values. Entrapment pressures calculated from this mean stress with the isotropic model for host- inclusion systems differ from the known experimental values by less than 0.2 GPa, which is of the order of the combined experimental uncertainties. These results show that the most significant effect of the elastic anisotropy of quartz is on the Raman shifts of the inclusion, and not on the subsequent calculation of entrapment conditions.

6.2 Introduction

Elastic geobarometry makes use of the contrast in elastic proprieties between host inclusion pairs to determine entrapment pressures for the inclusions.

When a host-inclusion pair is exhumed from depth to the Earth's surface non-lithostatic stresses are developed in the inclusion because of the contrast in their elastic properties (e.g. Rosenfeld and Chase, 1961). Current models for elastic geobarometry can only strictly be applied to the simple case of elastically isotropic host-inclusion pairs with ideal geometries consisting of a small inclusion trapped in an effectively infinite host (e.g. Angel et al., 2017, although corrections for the effects of the shape, geometry and elastic anisotropy of the inclusion on its stress state have been developed (Campomenosi et al., 2018; Mazzucchelli et al., 2018; Mazzucchelli et al., 2019)). Despite this intensive development of theory, an experimental validation of the calculated P and T of entrapment is still required. Such validation cannot come from measurements on inclusions in natural rocks because we do not know the exact P and T of entrapment, especially when there is evidence of over stepping of equilibrium reaction boundaries (e.g. Spear et al., 2014). An excellent way to assess the accuracy of inclusion geobarometry is to use synthetic host-inclusion pairs that can be produced with laboratory apparatus at controlled high- P and T conditions (e.g. Thomas and Spear, 2018).

In this paper we report measurements on quartz inclusions in almandine garnet synthesised at known P and T conditions in a piston-cylinder press. Quartz inclusions are very common inclusions in eclogitic garnets, and their elastic properties are relatively well-known. We used pure almandine as the garnet host because it is easier to synthesise large chemically-homogeneous crystals with quartz inclusions than some other garnets, and its elastic properties are known. We chose not to use garnets of intermediate compositions because their elastic properties are less-well defined than those of the end members. The equations of state reported by Angel et al. (2017) for quartz,

which includes the effects of the alpha-beta phase transition, and that of Milani et al. (2015) for almandine were used for all calculations. Facetted inclusions exhibit gradients in stress and strain. Therefore diffraction measurements of the entire inclusion only give some average value of strain over the whole inclusion that cannot be used in elastic geobarometry (e.g. Murri et al., 2018; Campomenosi et al., 2018). In contrast, Raman spectroscopy can probe small ‘spots’ inside inclusions and thus provide information about the variation of the stress and strain inside an inclusion. However, there are still several open questions concerning the method to determine “pressures” using Raman spectroscopy on inclusions, such as quartz, that are not elastically isotropic. We explore these issues and their influence on back-calculated entrapment conditions in this paper. In particular, for quartz inclusions the residual or remnant pressure (P_{inc}) has been determined in two different ways. One method (e.g. citeenami2007, ashley2016, thomas2018) is to assume that the quartz inclusions are under hydrostatic pressure. Then, the residual pressure of the inclusion can be determined from the shifts of the 464 cm^{-1} Raman mode of inclusions relative to free quartz, by using the hydrostatic calibration of Schmidt and Ziemann (2000). We demonstrate experimentally that this is incorrect for anisotropic inclusions, such as quartz, trapped in other minerals. When the quartz is trapped in a cubic host such as garnet the inclusion will be subject to isotropic strains imposed by the host and therefore, because it is elastically anisotropic, the inclusion will develop deviatoric (=non-hydrostatic) stresses. The change in the Raman band positions of a mineral is determined by the strain imposed on it (e.g. Grüneisen, 1926; Barron et al., 1980; Cantrell Jr, 1980; Angel et al., 2019), and therefore an inclusion crystal will exhibit Raman shifts that differ from those of a crystal subject to hydrostatic pressure. The strains on a quartz

inclusion crystal can be determined from the observed Raman shifts by using the phonon-mode Grüneisen tensors for quartz (Murri et al., 2018; Angel et al., 2019; Murri et al., 2019), from which one can determine the remnant or residual stress. We compare the residual quartz inclusion pressures calculated from this approach with those calculated assuming hydrostatic conditions for the inclusions. From these residual inclusion pressures we calculated the entrapment pressures using the equations of state of the host and the inclusions using the isotropic model for host-inclusion systems (e.g. Rosenfeld and Chase, 1961; Angel et al., 2017 and compared them to the known synthesis conditions. The results demonstrate the effect of the elastic anisotropy of quartz on the calculation of residual or remnant pressures and consequently on the accuracy of inferred entrapment pressures.

6.3 Methods

6.3.1 Piston-cylinder experiments

We synthesized garnet with quartz inclusions in end-loaded piston-cylinder devices at Syracuse University. Experiments were performed at typical eclogitic conditions during runs at 3.0 GPa and 775 °C (Alm-1; 72 hours) and at 2.5 GPa and 800 °C (Alm-2; 96 hours), following the approach outlined by Thomas and Spear (2018). Starting materials SiO₂ (amorphous), Al(OH)₃, FeO, Fe₃O₄, Fe₂O₃, FeTiO₃, and MnO (Alfa Aesar) were gently packed into silver capsules (see supplementary materials Table 6.7 for further information), and water was added to wet the powders completely. Crystallization of garnet required controlled oxygen fugacity. An assemblage of fayalite + magnetite + quartz contained in a separate adjacent capsule buffered the oxygen fugacity of the experiments. Approximately 10 mg of oxide mixtures and 5–8

mg H₂O were added to capsules (4 mm OD; 2.5 mm ID) used in 12.7 mm diameter NaCl-Pyrex-MgO piston-cylinder assemblies (Watson et al., 2002). We left 0.75 mm of headspace in the capsules to prevent contaminating the tops of the capsules with the starting materials. The fO₂ buffer capsule design developed for these experiments ((Trail et al., 2012) is identical to the principle of the classic internal capsule design (Jakobsson, 2012). In summary, platinum disks (150 μ m thick) were placed between the open ends of the buffer capsules and the capsules containing the garnet-producing oxide mixture (Thomas and Spear, 2018). Hydrogen diffusion across Pt disks that separated the garnet + quartz mineral assemblages from the oxygen buffer controlled (i.e. buffered) the oxygen pressure in the capsules. Temperatures were measured with D-type thermocouples (W97Re3–W75Re25), situated within 1 mm of the top of the capsule and are considered accurate to within 10 °C. The pressures in the piston–cylinder hydraulic rams were measured with Enerpac 140 MPa Bourdon-tube gauges with 18-cm-diameter dials. Experiments were cold pressurized to the desired run pressure followed by ramping the temperature at 100 °C/minute. Runs were quenched to below 100 °C in less than 60 s by turning off the furnace power. Pressure calibration of the piston cylinder is based on the quartz–coesite phase boundary (Boyd and England, 1960b; Kitahara and Kennedy, 1964), using the same assemblies as our experiments.

6.3.2 Sample quality assessment

After quenching the runs, the capsules were opened and successful runs were found to contain a mixture of free single crystals of garnet, and also other minerals, immersed in fluid. Single crystals were removed from the capsules and the garnet crystals were mounted in epoxy and polished by removing less

than 10 μm of garnet material. After polishing, the diameters of the garnet crystals were between 60 μm and 100 μm (Figs. 6.1a and e). By means of optical microscopy we selected only ideal inclusions to measure with Raman spectroscopy. An ideal inclusion must be isolated in a fracture-free garnet host, more than three inclusion radii from surfaces and other inclusions (e.g. Zhang, 1998; Mazzucchelli et al., 2018). Samples were also inspected using back scattered electron (BSE) imaging and characterized by electron microprobe analyses and maps using a JEOL JXA 8200 Superprobe equipped with five wavelength-dispersive (WDS) spectrometers and an energy dispersive (EDS) spectrometer (accelerating potential 15 kV, beam current 15 nA), at the Department of Earth Sciences, University of Milan. The phase assemblages of Alm-1 and Alm-2 are identical and show many similarities to some natural *HP* mineral assemblages, and consist of garnet, quartz, kyanite and ilmenite. The compositions of garnet crystals are essentially pure almandine (>99%, see Table 6.9). Inclusions in the garnets were quartz, rutile, kyanite and rarely ilmenite. Kyanite inclusions were mostly found as small inclusions in the cores of the garnets. The quartz inclusions range from sub-micrometer spherical inclusions to well-faceted inclusions 15 μm in maximum dimension. We observed that the garnet crystals in Alm-1 are slightly larger than those in Alm-2 (see Fig. 6.1). Quartz included in the garnet hosts of Alm-2 are commonly smaller and more numerous than quartz included in the garnet host of Alm-1.

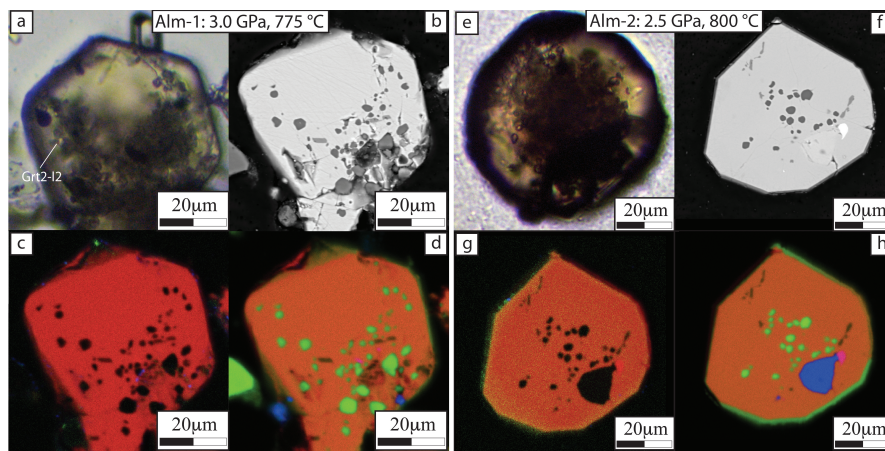


Figure 6.1: Optical microphotographs and SEM-BSE images of the samples Alm-1 synthesized at 3.0 GPa and 775 °C and Alm-2 synthesized at 2.5 GPa and 800 °C. (a,e) In optical microphotographs the garnets appear to be euhedral with several trapped inclusions. (b,f) Inclusions exposed on the surface are visible in the SEM-BSE images and therefore have not been used for further analyses. (c,g) Fe chemical element maps show that the almandine garnet is very homogeneous. (d,h) The combined Fe-Si-Ti chemical element maps in RGB show the different inclusion phases with quartz in green, rutile in blue and ilmenite in pink.

Raman peak positions (cm^{-1}) and wavenumber shifts (cm^{-1}) for quartz inclusions in garnet from experimental runs at 3.0 GPa and 775 °C.

	date	hosts	inclusions	wave numbers $\omega \text{ cm}^{-1}$						wave number shifts $\Delta\omega \text{ cm}^{-1}$								
				128 cm^{-1}	e.s.d.	206 cm^{-1}	e.s.d.	464 cm^{-1}	e.s.d.	128 cm^{-1}	e.s.d.	misfit	206 cm^{-1}	e.s.d.	misfit	464 cm^{-1}	e.s.d.	misfit
Alm-1	ideal inclusions																	
	12/5/18		I1	133.868	0.059	232.416	0.167	475.302	0.015	6.250	0.52	0.040	25.463	0.52	0.004	10.600	0.52	-0.032
	6/12/18		I2	132.878	0.266	231.051	0.360	474.503	0.041	5.643	0.52	-0.267	25.089	0.52	-0.024	10.432	0.52	0.214
	6/12/18	Grt1	I4	128.542	0.467	225.754	1.124	467.863	0.045	1.307	0.52	0.041	19.792	0.52	0.004	3.791	0.52	-0.033
	6/12/18		I5	133.722	0.171	232.654	0.296	474.918	0.034	6.487	0.52	0.132	26.692	0.52	0.012	10.846	0.52	-0.105
	6/12/18		I6	133.528	0.419	232.917	0.635	474.750	0.086	6.293	0.52	0.110	26.955	0.52	0.010	10.679	0.52	-0.088
	6/12/18		I1	131.968	0.306	229.953	0.861	470.771	0.058	4.733	0.52	0.935	23.992	0.52	0.085	6.699	0.52	-0.750
	12/5/18	Grt2	I2	133.908	0.098	231.747	0.319	474.897	0.027	6.290	0.52	0.223	24.793	0.52	0.020	10.196	0.52	-0.179
	6/12/18		I3	131.177	0.619	227.919	1.181	470.769	0.070	3.942	0.52	0.345	21.957	0.52	0.031	6.697	0.52	-0.276
	12/5/18		I1	133.855	0.161	230.241	0.420	472.453	0.027	6.237	0.52	1.296	23.287	0.52	0.118	7.751	0.52	-1.039
	12/5/18	Grt3	I2	134.292	0.056	233.304	0.163	474.911	0.073	6.674	0.52	0.535	26.350	0.52	0.049	10.209	0.52	-0.429
	6/12/18		I1	133.432	0.238	230.139	0.251	473.876	0.021	6.197	0.52	0.323	24.177	0.52	0.029	9.804	0.52	-0.259
	6/12/18	Grt4	I3	132.264	0.289	231.796	0.461	473.271	0.073	5.029	0.52	0.001	25.834	0.52	0.000	9.199	0.52	-0.001
	12/5/18	Grt5	I1	134.655	0.055	234.240	0.113	475.452	0.014	7.037	0.52	0.543	27.287	0.52	0.050	10.751	0.52	-0.436
	6/12/18	Grt6	I2	130.461	0.324	227.636	0.954	469.815	0.043	3.226	0.52	0.359	21.674	0.52	0.033	5.743	0.52	-0.288
	11/27/18		I1	132.750	0.098	228.930	0.141	472.781	0.012	4.765	0.52	0.328	22.968	0.52	0.030	7.871	0.52	-0.263
	11/27/18	Grt7	I3	134.328	0.090	232.656	0.295	475.499	0.032	6.343	0.52	0.169	26.694	0.52	0.016	10.589	0.52	-0.136
	non-ideal inclusions																	
6/12/18	Grt1	I3	131.534	0.376	223.810	0.691	471.938	0.039	4.299	0.52	-0.234	17.848	0.52	-0.021	7.867	0.52	0.188	
6/12/18	Grt2	I4	133.826	0.121	230.239	0.268	474.144	0.022	6.208	0.52	0.457	23.285	0.52	0.042	9.442	0.52	-0.366	
6/12/18	Grt4	I2	131.239	0.879	233.673	0.682	473.886	0.133	4.004	0.52	-0.815	27.711	0.52	-0.074	9.815	0.52	0.654	
6/12/18		I1	131.388	0.808	235.222	1.130	471.412	0.133	4.153	0.52	0.563	29.260	0.52	0.051	7.340	0.52	-0.451	
6/12/18	Grt6	I3	132.091	0.161	225.545	0.934	472.481	0.041	4.856	0.52	-0.064	19.583	0.52	-0.006	8.409	0.52	0.052	
6/12/18		I4	132.084	0.147	227.818	0.488	471.818	0.024	4.849	0.52	0.378	21.856	0.52	0.035	7.747	0.52	-0.303	
6/12/18		I2	134.341	0.101	234.468	0.225	475.360	0.029	6.356	0.52	0.344	28.506	0.52	0.031	10.451	0.52	-0.276	
6/12/18	Grt7	I4	134.111	0.305	233.130	0.260	474.523	0.035	6.126	0.52	0.538	27.169	0.52	0.049	9.613	0.52	-0.431	

Note: Wavenumber shifts and their estimated standard deviations (*e.s.d.*) have been obtained as described in the text. Not-ideal inclusions cannot be used to calculate the entrapment pressure. Not ideal inclusions show different Raman shifts, the problems can be a lot, for example they are partially exposed or to be close the host boundary or to be close fracture.

Raman peak positions (cm^{-1}) and wavenumber shifts (cm^{-1}) for quartz inclusions in garnet from experimental runs at 3.0 GPa and 775 °C.

	wave numbers ω cm^{-1}								wave number shifts $\Delta\omega$ cm^{-1}										
	date	hosts	inclusions	128 cm^{-1}	e.s.d.	206 cm^{-1}	e.s.d.	464 cm^{-1}	e.s.d.	128 cm^{-1}	e.s.d.	misfit	206 cm^{-1}	e.s.d.	misfit	464 cm^{-1}	e.s.d.	misfit	
Alm-2	ideal inclusions																		
	12/7/18	Grt1	I1	132.774	0.041	228.331	0.088	472.838	0.008	4.904	0.52	0.2347	21.448	0.52	0.0215	8.057	0.52	-0.188	
	12/8/18		I2	131.907	0.042	226.990	0.080	472.279	0.006	4.037	0.52	-0.088	20.107	0.52	-0.008	7.498	0.52	0.0705	
	12/9/18		I3	132.572	0.060	227.852	0.186	472.449	0.012	4.703	0.52	0.2766	20.968	0.52	0.0252	7.667	0.52	-0.222	
	6/13/18	Grt2	I5	131.705	0.102	227.078	0.224	472.206	0.017	3.737	0.52	-0.249	19.767	0.52	-0.023	7.416	0.52	0.2001	
	12/5/18	Grt3	I1	132.511	0.058	228.470	0.183	473.254	0.019	4.641	0.52	-0.114	21.587	0.52	-0.01	8.473	0.52	0.0915	
	12/5/18		I2	132.481	0.059	228.348	0.214	473.160	0.017	4.611	0.52	-0.096	21.464	0.52	-0.009	8.379	0.52	0.0769	
	12/7/18	Grt4	I1	132.591	0.042	225.216	0.070	472.205	0.008	4.721	0.52	0.2646	18.333	0.52	0.0243	7.423	0.52	-0.212	
	12/7/18		I2	132.723	0.032	227.654	0.117	473.099	0.008	4.853	0.52	0.0407	20.770	0.52	0.0038	8.318	0.52	-0.033	
	12/7/18	Grt5	I1	132.854	0.042	227.263	0.053	472.951	0.006	4.985	0.52	0.1707	20.380	0.52	0.0155	8.170	0.52	-0.137	
	12/5/18	Grt6	I1	132.413	0.047	227.041	0.234	472.357	0.015	4.543	0.52	0.1788	20.158	0.52	0.0164	7.576	0.52	-0.143	
	12/7/18	Grt7	I1	132.377	0.058	226.707	0.137	472.359	0.010	4.508	0.52	0.1419	19.824	0.52	0.013	7.578	0.52	-0.114	
	6/13/18	Grt8	I2	130.914	0.209	227.137	1.184	471.827	0.046	2.946	0.52	-0.54	19.826	0.52	-0.049	7.037	0.52	0.433	
	11/22/18	Grt9	I2	132.164	0.162	226.978	0.273	472.572	0.021	4.196	0.52	-0.151	19.667	0.52	-0.014	7.782	0.52	0.1213	
	11/22/18		I1	133.222	0.067	229.171	0.283	473.518	0.024	5.254	0.52	0.1438	21.860	0.52	0.0131	8.728	0.52	-0.115	
	11/22/18	Grt1	I2	132.391	0.079	227.980	0.249	472.598	0.066	4.422	0.52	0.0225	20.669	0.52	0.002	7.808	0.52	-0.018	
	11/22/18		I1	133.301	0.043	229.476	0.156	473.573	0.017	5.332	0.52	0.1845	22.164	0.52	0.0168	8.783	0.52	-0.148	
	non-ideal inclusions																		
	6/13/18	Grt2	I4	131.462	0.165	226.831	0.278	472.199	0.019	3.493	0.52	-0.41	19.520	0.52	-0.037	7.409	0.52	0.3286	
6/13/18	I7		130.954	0.059	222.136	0.098	470.469	0.011	2.986	0.52	-0.131	14.825	0.52	-0.012	5.679	0.52	0.1054		
12/7/18	Grt4	I3	133.370	0.050	229.798	0.119	474.289	0.010	5.500	0.52	-0.025	22.915	0.52	-0.002	9.508	0.52	0.0202		
12/5/18	Grt6	I2	133.223	0.050	229.927	0.150	473.721	0.014	5.353	0.52	0.1674	23.044	0.52	0.0153	8.940	0.52	-0.134		
11/22/18	Grt9	I1	132.809	0.227	230.383	0.534	474.276	0.050	4.841	0.52	-0.407	23.072	0.52	-0.037	9.486	0.52	0.3264		
11/22/18		I3	133.353	0.115	230.690	0.355	473.992	0.033	5.384	0.52	0.0781	23.379	0.52	0.0072	9.202	0.52	-0.063		
11/22/18	Grt10	I3	133.431	0.083	229.832	0.086	473.803	0.008	5.462	0.52	0.1714	22.520	0.52	0.0156	9.013	0.52	-0.137		
11/22/18	Grt11	I2	132.998	0.047	229.855	0.158	473.749	0.013	5.029	0.52	-0.064	22.544	0.52	-0.006	8.959	0.52	0.051		

Note: Wavenumber shifts and their estimated standard deviations (*e.s.d.*) have been obtained as described in the text. Not-ideal inclusions cannot be used to calculate the entrapment pressure. Not ideal inclusions show different Raman shifts, the problems can be a lot, for example they are partially exposed or to be close the host boundary or to be close fracture.

6.3.3 Raman spectroscopy measurements

The inclusions were measured using parallel-polarized Raman spectra in backscattering geometry with a Horiba Jobin-Yvon T64000 triple-monochromator spectrometer (spectral resolution of 2 cm^{-1} , instrumental accuracy in peak positions of 0.52 cm^{-1} $1\text{ }\mu\text{m}$ spot size) with a 532 nm green laser. All of the measurements were performed at 20°C and room pressure. For calibration we used the Raman band of silicon metal whose theoretical peak position is 520.7 cm^{-1} . We collected Raman spectra over several days, and several times each day we measured the Raman spectrum of a free quartz crystal to have a reference spectrum in order to have good control over instrumental uncertainties and stability (see Table 6.8). All reference spectra were measured with 3 acquisitions of 15 seconds each. The peak positions of quartz references acquired in the same day differ by less than the instrumental uncertainty. Raman spectra were acquired using a laser spot of $1\text{ }\mu\text{m}$ focused on the center of inclusions because this is the point where the stress and strain are least disturbed by the shape of the inclusion (Campomenosi et al., 2018). We measured several inclusions in several single garnet host crystals, and on some inclusions we repeated the measurement over several days to estimate the reproducibility of the measurements. Overall, we collected data on more than 20 inclusions per experiment. All inclusion spectra were measured with 5 acquisitions of 40 seconds each. Raman spectra were fitted with the OriginPro 2018b software using a B-spline as a baseline correction and pseudo-Voigt peak functions Raman. The estimated uncertainties on fitted peak positions were commonly $< 0.30\text{ cm}^{-1}$. We therefore used the instrumental accuracy (0.52 cm^{-1}) as a conservative estimated of the standard deviation of the peak positions. The stress-induced shift of the Raman peaks of the inclusions (tables 6.1 and 6.2) were determined from the difference in their

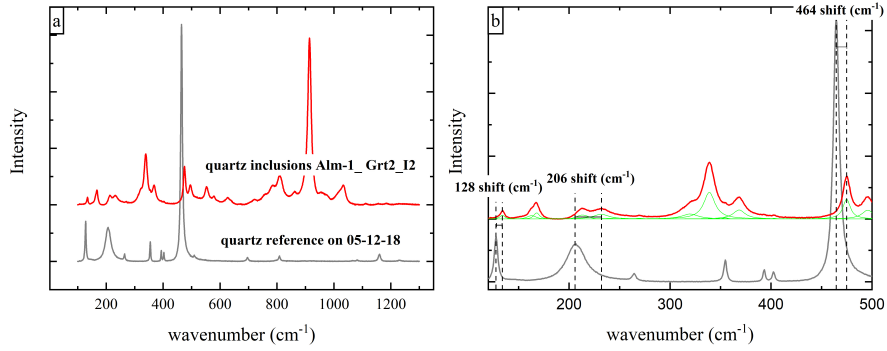


Figure 6.2: (a) Raman spectrum of quartz reference and quartz inclusion in garnet (Alm-1_Grt2_I2). (b) Detail of the spectra around the 128, 206 and 464 cm^{-1} Raman bands showing the individual peak components. The green line shows the components of the fitted spectrum.

positions from those of the quartz standard crystal measured in the same measurement session. This avoids any problems of long-term instabilities of the instrument.

6.4 Results and discussion

6.4.1 Raman wavenumber shift, inclusion pressure and strain

We explored several methods to calculate the residual pressure of quartz inclusions while still trapped in garnet. All of them depend on the difference $\Delta\omega$ between the wavenumbers (measured in cm^{-1}) of the Raman peaks of the inclusion and those of the same peaks measured from the free crystal of quartz used as a standard. As shown in Fig. 6.2 the dashed lines highlight the peak position for the measured inclusion and for the standard unstrained crystal. the shift of the Raman shift ($\Delta\omega$) is calculated as the difference

between the band position for these two values for each of the well defined peaks (e.g. 128, 206, 464 cm^{-1} in our case). The most widely-used method in the literature (e.g. Enami et al., 2007; Ashley et al., 2016) is simply to interpret the measured $\Delta\omega$ of the 464 cm^{-1} Raman band of quartz as the consequence of hydrostatic pressure in the inclusion, by using the hydrostatic calibration by Schmidt and Ziemann (2000):

$$P_{inc}^{464} \text{MPa} = 0.36079[(\Delta\omega_{P464})]^2 + 110.86(\Delta\omega_{464})$$

A similar calibration can be used to determine the hydrostatic pressure of a quartz crystal from the shift of the 206 cm^{-1} Raman band in quartz (Grüneisen, 1926):

$$P_{inc}^{206} \text{MPa} = 0.4633[(\Delta\omega_{P206})]^2 + 31.66(\Delta\omega_{464})$$

Fig. 6.3 shows a plot of the values of P_{inc}^{206} against P_{inc}^{464} for each of the measured inclusions. The data should plot along a 1:1 line if the pressure in the inclusions is hydrostatic. The difference between the two ‘pressures’ is small in the inclusions synthesised in the lower-pressure experiment (Alm-2), and these inclusions have P_{inc}^{464} (Fig. 6.4b) that are within 0.1 GPa of the expected P_{inc} calculated from the known synthesis P and T and the equations of state of almandine and quartz using the isotropic host-inclusion model for spherical inclusions (Angel et al., 2014b; Angel et al., 2017). However, for the inclusions synthesised in the higher-pressure experiment (Alm-1) the values of P_{inc}^{464} range from 0.4 GPa to 1.2 GPa, and P_{inc}^{206} from 0.8 to 1.2 GPa (Fig. 6.3). This indicates the presence of significant non-hydrostatic stress in these inclusions, which has different effects on the shifts of the two Raman bands (Murri et al., 2019). The consequence is that the P_{inc}^{464} from the inclusions of

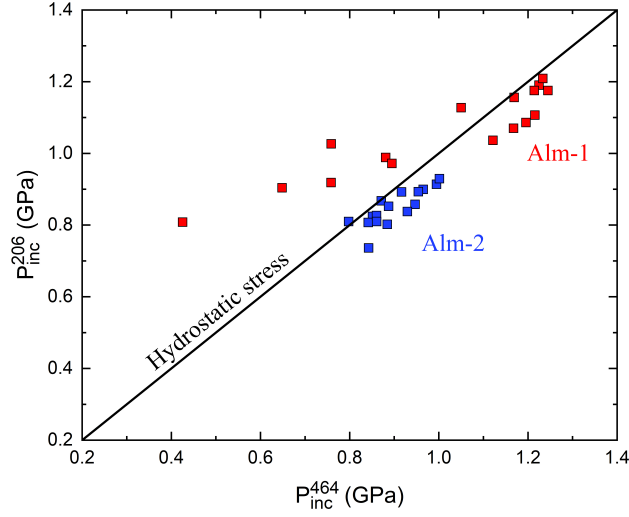


Figure 6.3: Pressures indicated by the 206 and 464 cm^{-1} Raman bands in inclusions, as calculated with the 17 hydrostatic calibration of Schmidt and Ziemann (2000). The deviation of the points from the 1:1 line indicates the presence of non-hydrostatic stresses in the inclusions.

this experiment (Fig. 6.4a) deviates by up to 0.7 GPa from the value of P_{inc} expected from the isotropic model of host-inclusion systems. Changes in the Raman shifts (phonon frequencies or wavenumbers) of a crystal arise from strains imposed upon it (e.g. Grüneisen, 1926; Barron et al., 1980; Cantrell Jr, 1980; Angel et al., 2019). The relationship between the change in the position of each Raman peak position and the imposed strain is defined by the values of the components of the phonon- mode Grüneisen tensor, which are different for each mode in a crystal. The values of the phonon-mode Grüneisen tensors of quartz were determined by Murri et al. (2019). The strains of the quartz inclusions relative to a free quartz crystal in air can therefore be determined from the shifts of the Raman lines $\Delta\omega$ relative to the free quartz crystal. Quartz is trigonal and therefore only two symmetry-independent strains, $\varepsilon_1 = \varepsilon_2$, representing the strains along the a and b axes

of the unit cell, and the strain ε_3 (the strain along the c-axis) can be determined (Angel et al., 2019). In order to determine the two independent strains ($\Delta\omega$ from at least two Raman peaks from each inclusion. The problem with this approach, as demonstrated by Murri et al. (2018), is that the slopes of the iso-shift lines for the Raman bands that can be measured on quartz inclusions trapped in almandine garnet are almost parallel to one another and are nearly parallel to the isochors. As a consequence the correlation between the values of ε_1 and ε_3 obtained in this way is very high (90-99%). The correlation makes it challenging to determine a unique combination of strains ε_1 and ε_3 from the measured Raman peak positions, and the small differences in Raman peak positions measured from a series of inclusions trapped under the same conditions leads to a spread in strains that lies sub-parallel to the isochors (Fig. 6.5a). To try to minimize the effects of this correlation we performed a series of tests to select the most reliable Raman bands (at least 3 bands) for the calculations of the strain components. As no significant improvement has been found using different combinations of bands (128, 206, 264, 464, 696, 1162 cm^{-1}) with the correlations between the strains always greater than 90%, we restricted our analyses to the three bands with consistently small instrumental and fitting uncertainties, i.e. those at 128, 206 and 464 cm^{-1} . As a practical illustration of the effects of correlation, we show in Fig. 6.5b the strains calculated from the measured Raman peak positions of the three modes, each adjusted from the measured values by ± 2 estimated standard deviations (e.s.d.) of their values. The resulting strains (Fig. 6.5b) are spread in the same way as the measurements of the different inclusions (Fig. 6.5a), strongly suggesting that the spread in strain values arises from the uncertainties in the measurements of Raman peak positions. Because the correlation between the strains ε_1 and ε_3 determined in this way

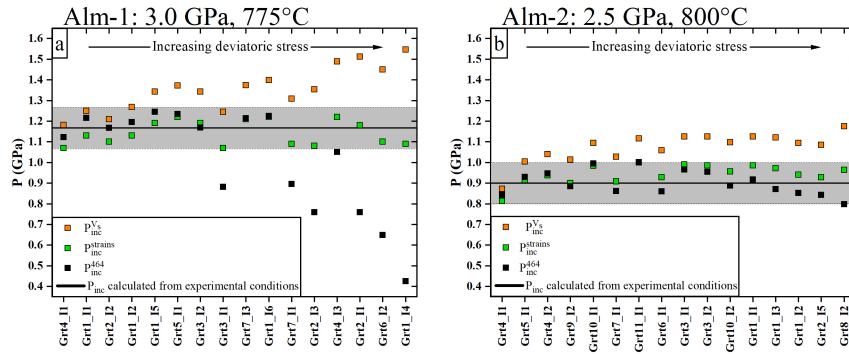


Figure 6.4: Inclusion pressures calculated for the quartz inclusions in garnet from synthesis at (a) 3.0 GPa and (b) 2.5 GPa. The black line represents the inclusion pressure (P_{inc}) calculated from the synthesis conditions with the isotropic host-inclusion model, and the shaded area represents the maximum uncertainties of the calculation. Values of P^{464}_{inc} calculated with the hydrostatic calibration (black) show a much larger discrepancy than $P^{strains}_{inc}$ obtained from the strain components (green) for experiment at 3.0 GPa (Alm-1), but the methods agree for the experiments at 2.5 GPa. The P^{464}_{inc} (orange) show a systematic overestimate of inclusion pressure compared to that calculated from the synthesis conditions.

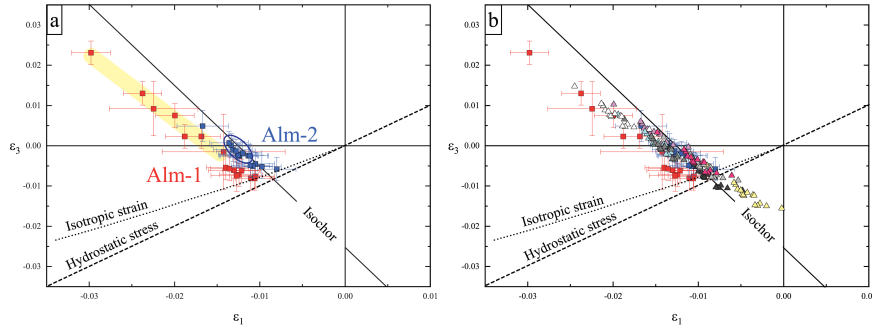


Figure 6.5: (a) Strain components determined at room temperature for quartz inclusions from experiments Alm-1 (red squares) and Alm-2 (blue squares). The values of the strains from both experiments lie almost parallel to the isochors and are clustered close to, but clearly above, the strains for hydrostatic conditions. The spread in values for the 2.5 GPa experiment is much smaller than that for the inclusions synthesised at 3.0 GPa. The yellow area indicates the inclusions in Alm-1 that have discrepancies in P_{inc}^{464} larger than the experimental uncertainties. In (b) we report strains (yellow triangles) of 11 inclusions that are inside the blue circle of part (a), calculated from the peak positions of the Raman bands adjusted by different combinations of ± 1 or 2 estimated standard deviations (*e.s.d.*). The spread in the resulting strains shows that the measured spread between inclusions arises mostly from the uncertainties in Raman peak positions.

is negative and quasi- parallel to the isochors (Fig. 6.5), the estimated uncertainties on the individual strain values are significantly greater than the estimated uncertainty on the value of the volume strain $\varepsilon_V = 2\varepsilon_1 + \varepsilon_3$ (Table 6.2). In other words, the volume strain is more precisely determined than the individual values of the strain. The residual inclusion pressure calculated from the volume strain (which we distinguish as PV_s) by using the hydrostatic EoS of quartz (Angel et al., 2017) is generally too high P (Fig. 6.4). The deviations are greater for inclusions in experiment Alm-1 where they are overestimated by up to 0.45 GPa (Fig. 6.4a). And the further the inclusion stress and strain state are from hydrostatic conditions, the higher the calculated PV_s . This is because the effective bulk modulus of quartz, defined as $K = \frac{(-dP)}{\varepsilon_V}$ decreases along an isochor from isostrain conditions (the Voigt bound on the bulk modulus) to hydrostatic conditions (the Reuss bound) and continues to decrease as the ε_1 strain becomes more negative (and ε_3 becomes more positive). For the most extreme strain condition measured (in inclusion Grt1_I4 in sample Alm-1), the bulk modulus is only 30 GPa, compared to a value of 37 GPa for hydrostatic conditions. As a consequence, the use of the hydrostatic bulk modulus (Reuss bound) to calculate the inclusion pressures as $PV_s = -\varepsilon_V K_{Reuss}$ overestimates the true residual inclusion pressure. The components of stress, σ_i , in the inclusion can be determined from the measured strains by using the matrix relationship $\sigma_i = c_{ij}\varepsilon_j$, in which c_{ij} is the elastic modulus matrix (*Physical Properties of Crystals*, (1957), 142). Because only the strains $\varepsilon_1 = \varepsilon_2$ and ε_3 are non-zero in the inclusion, there are no shear strains, and only the normal stress components ($\sigma_1 = \sigma_2$ and σ_3) are non-zero. We use the elastic moduli of quartz determined at room pressure by Wang et al. (2015). From these calculated stresses in the inclusion we calculate the $P_{strains}$ as the mean stress, $\frac{2\sigma_1 + \sigma_3}{3}$. With this calculation the

discrepancy between the measured P_{strains} and the theoretical P_{inc} calculated with the isotropic model from our synthesis conditions are smaller than 0.1 GPa (Table 6.5, Figs. 6.6 and 6.4). As shown in Fig. 6.4b no significant improvement was observed in the distribution of the residual pressures for the inclusions from the low-pressure experiment (Alm-2). They are similar to the deviations of P_{464} which is calculated from the shift of only the 464 cm^{-1} line. Conversely for the higher-P synthesis (Alm-1), while the deviation from the expected residual pressures using the strain method remains identical to that of the low-P runs, the deviations for the values calculated using the 464 cm^{-1} line are more than 7 times larger (e.g. up to 0.7 GPa). These results clearly show that the errors in P_{inc} obtained by using the hydrostatic calibration of the 464 cm^{-1} line become worse at higher inclusion pressures.

Calculated strains for quartz inclusions in garnet from experimental runs at 3.0 GPa and 775 °C.

	date	host	inclusion	$\epsilon_1 + \epsilon_2$	e.s.d.	ϵ_3	e.s.d.	ϵ_V	e.s.d.	Covariance ($\times 10^{-6}$)	Correlation (%)	χ^2
Alm-1	ideal inclusions											
	12/5/18		I1	-0.0221	0.00451	-0.0081	0.00291	-0.0302	-0.00168	-12.99447	-99	0.01
	6/12/18		I2	-0.0243	0.00451	-0.0062	0.00291	-0.0305	0.00168	-12.99447	-99	0.43
	6/12/18	Grt1	I4	-0.0596	0.00451	0.0231	0.00291	-0.0365	0.00168	-12.99447	-99	0.01
	6/12/18		I5	-0.0249	0.00451	-0.0072	0.00291	-0.0322	0.00168	-12.99447	-99	0.11
	6/12/18		I6	-0.0280	0.00451	-0.0054	0.00291	-0.0333	0.00168	-12.99447	-99	0.07
	6/12/18		I1	-0.0449	0.01041	0.0092	0.00673	-0.0358	0.00387	-69.3447	-99	5.34
	12/5/18	Grt2	I2	-0.0212	0.00451	-0.0081	0.00291	-0.0293	0.00168	-12.99447	-99	0.3
	6/12/18		I3	-0.0399	0.00451	0.0075	0.00291	-0.0324	0.00168	-12.99447	-99	0.73
	12/5/18		I1	-0.0285	0.01443	-0.0015	0.00932	-0.0300	0.00537	-	-99	10.3
	12/5/18	Grt3	I2	-0.0261	0.00596	-0.0061	0.00385	-0.0322	0.00222	-22.7348	-99	1.75
	6/12/18		I1	-0.0211	0.00451	-0.0076	0.00291	-0.0287	0.00168	-12.99447	-99	0.64
	6/12/18	Grt4	I3	-0.0376	0.00451	0.0023	0.00291	-0.0353	0.00168	-12.99447	-99	0
	12/5/18	Grt5	I1	-0.0254	0.00605	-0.0074	0.00391	-0.0328	0.00225	-23.43685	-99	1.8
	6/12/18	Grt6	i2	-0.0475	0.00451	0.0130	0.00291	-0.0345	0.00168	-12.99447	-99	0.79
	11/27/18		I1	-0.0337	0.00451	0.0023	0.00291	-0.0314	0.00168	-12.99447	-99	0.66
	11/27/18	Grt7	I3	-0.0271	0.00451	-0.0057	0.00291	-0.0328	0.00168	-12.99447	-99	0.17
	non-ideal inclusions											
	6/12/18	Grt1	I3	-0.01341	0.00451	-0.00712	0.00291	-0.02053	0.00168	-12.99447	-99	0.33
	6/12/18	Grt2	I4	-0.01916	0.00509	-0.00807	0.00329	-0.02723	0.00189	-16.54769	-99	1.27
	6/12/18	Grt4	I2	-0.04741	0.00908	0.00734	0.00586	-0.04007	0.00338	-52.71545	-99	4.06
	6/12/18		I1	-0.06742	0.00627	0.01991	0.00405	-0.04751	0.00233	-25.12627	-99	1.93
	6/12/18	Grt6	I3	-0.01527	0.00451	-0.00741	0.00291	-0.02268	0.00168	-12.99447	-99	0.03
	6/12/18		I4	-0.02906	0.00451	0.0001	0.00291	-0.02896	0.00168	-12.99447	-99	0.87
	6/12/18		I2	-0.0358	0.00451	-0.00135	0.00291	-0.03714	0.00168	-12.99447	-99	0.72
	6/12/18	Grt7	I4	-0.03574	0.00599	-0.00014	0.00387	-0.03588	0.00223	-22.97464	-99	1.77

Note: Strains and their estimated standard deviations (*e.s.d.*) have been calculated with the Strainman software (Angel et al., 2019) as described in the text.

Calculated strains for quartz inclusions in garnet from experimental runs at 3 GPa and 775 °C.

	date	host	inclusion	$\epsilon_1 + \epsilon_2$	e.s.d.	ϵ_3	e.s.d.	ϵ_V	e.s.d.	Covariance ($\times 10^6$)	Correlation (%)	χ^2
Alm-2	ideal inclusions											
	12/7/18		I1	-0.0252	0.00451	-0.00218	0.00291	-0.0274	0.00168	-12.9945	-99	0.34
	12/8/18	Grt1	I2	-0.0267	0.00451	0.00004	0.00291	-0.0267	0.00168	-12.9945	-99	0.05
	12/9/18		I3	-0.0263	0.00451	-0.001	0.00291	-0.0273	0.00168	-12.9945	-99	0.47
	6/13/18	Grt2	I5	-0.0272	0.00451	0.00063	0.00291	-0.0265	0.00168	-12.9945	-99	0.38
	12/5/18	Grt2	I1	-0.0248	0.00451	-0.00262	0.00291	-0.0275	0.00168	-12.9945	-99	0.08
	12/5/18		I2	-0.0250	0.00451	-0.00244	0.00291	-0.0274	0.00168	-12.9945	-99	0.06
	12/7/18	Grt4	I1	-0.0160	0.00451	-0.00574	0.00291	-0.0217	0.00168	-12.9945	-99	0.43
	12/7/18		I2	-0.0210	0.00451	-0.00449	0.00291	-0.0255	0.00168	-12.9945	-99	0.01
	12/7/18	Grt5	I1	-0.0195	0.00451	-0.00517	0.00291	-0.0247	0.00168	-12.9945	-99	0.18
	12/5/18	Grt6	I1	-0.0240	0.00451	-0.00185	0.00291	-0.0259	0.00168	-12.9945	-99	0.2
	12/7/18	Grt7	I1	-0.0227	0.00451	-0.00247	0.00291	-0.0252	0.00168	-12.9945	-99	0.12
	6/13/18	Grt8	I2	-0.0334	0.00601	0.00491	0.00388	-0.0285	0.00224	-23.131	-99	1.78
	11/22/18	Grt9	I2	-0.0224	0.00451	-0.00254	0.00291	-0.0250	0.00168	-12.9945	-99	0.14
	11/22/18		I1	-0.0216	0.00451	-0.00511	0.00291	-0.0267	0.00168	-12.9945	-99	0.13
	11/22/18	Grt10	I2	-0.0256	0.00451	-0.00126	0.00291	-0.0268	0.00168	-12.9945	-99	0
	11/22/18	Grt11	I1	-0.0222	0.00451	-0.00493	0.00291	-0.0272	0.00168	-12.9945	-99	0.21
	non-ideal inclusions											
	6/13/18	Grt2	I4	-0.0273	0.00456	0.00097	0.00295	-0.0263	0.0017	-13.3217	-99	1.03
	6/13/18		I7	-0.0188	0.00451	-0.00062	0.00291	-0.0194	0.00168	-12.9945	-99	0.11
	12/7/18	Grt4	I3	-0.0206	0.00451	-0.00675	0.00291	-0.0274	0.00168	-12.9945	-99	0
	12/5/18	Grt6	I2	-0.0251	0.00451	-0.00374	0.00291	-0.0289	0.00168	-12.9945	-99	0.17
	11/22/18	Grt9	I1	-0.0247	0.00453	-0.00413	0.00293	-0.0288	0.00169	-13.1354	-99	1.01
	11/22/18		I3	-0.0250	0.00451	-0.00414	0.00291	-0.0291	0.00168	-12.9945	-99	0.04
	11/22/18	Grt10	I3	-0.0219	0.00451	-0.0055	0.00291	-0.0274	0.00168	-12.9945	-99	0.18
	11/22/18	Grt11	I2	-0.0244	0.00451	-0.00382	0.00291	-0.0282	0.00168	-12.9945	-99	0.02

Note: Strains and their estimated standard deviations (*e.s.d.*) have been calculated with the Strainman software (Angel et al., 2019) as described in the text.

6.4.2 Calculation of entrapment conditions

From the residual inclusion pressures P_{inc} obtained by the three approaches we calculated inclusion entrapment pressures P_{trap} at the known synthesis T , with the EosFit- P_{inc} software (Angel et al., 2017), which implements the isotropic spherical model for host-inclusion systems.

The following results are based on the isotropic model for both the relaxation and the thermodynamic calculation (see Angel et al., 2014b; Angel et al., 2017 for details). As could be expected from the results shown in Fig. 6.4, the $P_{\text{trap}}^{\text{strains}}$ (Fig. 6.6) derived from the measurements of strain are in good agreement with the experimental pressures of synthesis for both experiments. The values of P_{trap}^{Vs} obtained from the volume strain are always overestimated compared to experimental pressure, the values of P_{inc}^{Vs} are too high for the reasons explained above. When the strains of the inclusions are close to those for hydrostatic stress the overestimation is small, but it increases with increasing deviatoric stress in the inclusion. On the other hand, the values of P_{trap}^{464} , which are derived from the hydrostatic calibration of the Raman shifts, only agree with the experimental synthesis conditions for the experiment at 2.5 GPa (Fig. Fig. 6.6b). For the experiment at 3 GPa, although some of the P_{trap}^{464} values are correct, the maximum discrepancy is about 1.2 GPa (Fig. 6.6a). This spread in pressure is far greater than the expected uncertainties. The difference between P_{trap} calculated using the two approaches is greater for the inclusions whose strains deviate most (yellow area in Fig. 6.5) from those expected for hydrostatic stress, indicating that the source of the errors in P_{trap}^{464} comes from ignoring the effect on Raman shifts of non-hydrostatic stresses in the inclusions.

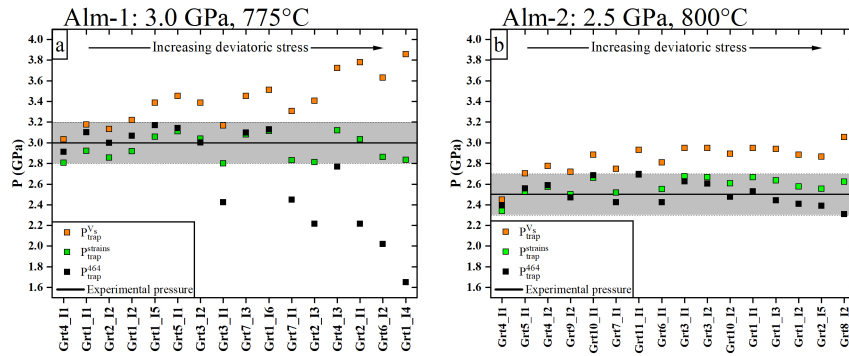


Figure 6.6: Entrapment pressures calculated for the quartz inclusions in garnet from synthesis at (a) 3.0 GPa and (b) 2.5 GPa. The black line represents the experimental pressure (P_{trap}) of the synthesis conditions for quartz trapped in almandine garnet and the shaded area represents the maximum estimated uncertainty propagated through the calculation of P_{trap} . The uncertainty of the calibration of the piston cylinder is less than 0.02 GPa. $P_{\text{traps}}^{\text{strains}}$ obtained from P_{trap}^{464} are represented by green squares and are in good agreement with experimental entrapment pressures for both experiments. P_{trap}^{464} (black) calculated from P_{inc}^{464} show a good agreement in the experiments at lower pressure and much larger spread in values in the experiment at higher pressure; the P_{trap}^{464} values outside the uncertainty band are from the inclusions highlighted in yellow in Fig. 6.5a. The $P_{\text{trap}}^{V_s}$ (orange) show a systematic overestimation of inclusion pressure (P_{inc}) compared to that calculated from the synthesis conditions.

Principal stress components ($\sigma_1=\sigma_2$ and σ_3), inclusion pressures (P_{inc}) and entrapment pressures (P_{trap}) calculated for quartz inclusions in garnet from experimental runs at 3 GPa and 775 °C.

	From 206 wavenumber shift				From 464 wavenumber shift		From strain components				From volume strain		
	date	hosts	inclusions	P_{inc}^{206} (GPa)	P_{trap}^{206} (GPa)	P_{inc}^{464} (GPa)	P_{trap}^{464} (GPa)	$\sigma_1=\sigma_2$ (GPa)	σ_3 (GPa)	$P_{inc}^{strains} = -\langle \sigma \rangle$ (GPa)	$P_{trap}^{strains}$ (GPa)	P_{inc}^{Vs} (GPa)	$P_{trap}^{Vs}(GPa)$
Alm-1	ideal inclusions												
	12/5/18		I1	1.11	2.87	1.22	3.10	-1.13	-1.14	1.13	2.92	1.25	3.18
	6/12/18		I2	1.09	2.83	1.20	3.07	-1.21	-0.96	1.13	2.92	1.27	3.22
	6/12/18	Grt1	I4	0.81	2.47	0.43	1.65	-2.49	1.72	1.09	2.83	1.55	3.86
	6/12/18		I5	1.18	3.02	1.24	3.17	-1.25	-1.08	1.19	3.06	1.34	3.39
	6/12/18		I6	1.19	3.05	1.22	3.13	-1.37	-0.92	1.22	3.11	1.40	3.51
	6/12/18		I1	1.03	2.22	0.76	2.22	-1.98	0.42	1.18	3.03	1.51	3.78
	12/5/18	Grt2	I2	1.07	2.80	1.17	3.00	-1.09	-1.12	1.10	2.86	1.21	3.09
	6/12/18		I3	0.92	2.50	0.76	2.21	-1.77	0.30	1.08	2.81	1.35	3.41
	12/5/18		I1	0.99	2.63	0.88	2.42	-1.35	-0.51	1.07	2.80	1.24	3.17
	12/5/18	Grt3	I2	1.16	2.98	1.17	3.00	-1.29	-0.97	1.19	3.04	1.34	3.39
	6/12/18		I1	1.04	2.73	1.12	2.91	-1.08	-1.07	1.07	2.81	1.18	3.03
	6/12/18	Grt4	I3	1.13	2.92	1.05	2.77	-1.72	-0.22	1.22	3.12	1.49	3.72
	12/5/18	Grt5	I1	1.21	3.09	1.23	3.14	-1.28	-1.10	1.22	3.11	1.37	3.45
	6/12/18	Grt6	i2	0.90	2.47	0.65	2.02	-2.05	0.80	1.10	2.86	1.45	3.63
	11/27/18		I1	0.97	2.60	0.89	2.45	-1.54	-0.18	1.09	2.83	1.31	3.31
	11/27/18	Grt7	I3	1.18	3.02	1.21	3.10	-1.34	-0.95	1.21	3.08	1.37	3.45
	non-ideal inclusions												
	6/12/18	Grt1	I3	0.71	2.11	0.89	2.47	-0.71	-0.92	0.78	2.24	0.82	2.31
	6/12/18	Grt2	I4	0.99	2.63	1.08	2.81	-0.99	-1.10	1.03	2.71	1.12	2.89
	6/12/18	Grt4	I2	1.23	3.14	1.12	2.92	-2.12	0.19	1.35	3.40	1.72	4.29
	6/12/18		I1	1.32	2.35	0.83	2.35	-2.90	1.28	1.51	3.76	2.09	5.30
	6/12/18	Grt6	I3	0.80	2.26	0.96	2.59	-0.80	-0.98	0.86	2.39	0.92	2.49
	6/12/18		I4	0.91	2.49	0.88	2.44	-1.35	-0.35	1.02	2.69	1.20	3.06
	6/12/18		I2	1.28	3.24	1.20	3.07	-1.69	-0.59	1.32	3.34	1.58	3.94
	6/12/18	Grt7	I4	1.20	3.08	1.10	2.87	-1.67	-0.46	1.27	3.21	1.52	3.79

Note: Principal stress components and values of P_{inc} have been calculated from the strains using the full elastic tensor by Wang et al. (2015) as described in the text. P_{trap} values have been calculated using EosFit- P_{inc} (Angel et al., 2017). Non-ideal inclusions exhibit significantly different values of both P_{inc} and P_{trap} .

Principal stress components ($\sigma_1=\sigma_2$ and σ_3), inclusion pressures (P_{inc}) and entrapment pressures (P_{trap}) calculated for quartz inclusions in garnet from experimental runs at 2.5 GPa and 800 °C.

	From 206 wavenumber shift				From 464 wavenumber shift		From strain components				From volume strain		
	date	hosts	inclusions	P_{inc}^{206} (GPa)	P_{trap}^{206} (GPa)	P_{inc}^{464} (GPa)	P_{trap}^{464} (GPa)	$\sigma_1=\sigma_2$ (GPa)	σ_3 (GPa)	$P_{inc}^{strains} = -\langle \sigma \rangle$ (GPa)	$P_{trap}^{strains}$ (GPa)	P_{inc}^{Vs} (GPa)	P_{trap}^{Vs} (GPa)
Alm-2	ideal inclusions												
	12/7/18		I1	0.89	2.48	0.92	2.53	-1.20	-0.54	0.98	2.67	1.13	2.95
	12/8/18	Grt1	I2	0.82	2.36	0.85	2.41	-1.25	-0.33	0.94	2.58	1.09	2.89
	12/9/18		I3	0.87	2.44	0.87	2.44	-1.24	-0.43	0.97	2.64	1.12	2.94
	6/13/18	Grt2	I5	0.81	2.32	0.84	2.39	-1.26	-0.27	0.93	2.56	1.09	2.87
	12/5/18		I1	0.90	2.50	0.97	2.63	-1.19	-0.59	0.99	2.68	1.13	2.95
	12/5/18	Grt3	I2	0.89	2.49	0.95	2.61	-1.19	-0.57	0.99	2.67	1.13	2.95
	12/7/18		I1	0.74	2.19	0.84	2.39	-0.82	-0.81	0.81	2.34	0.87	2.45
	12/7/18	Grt4	I2	0.86	2.42	0.95	2.59	-1.04	-0.74	0.94	2.57	1.04	2.78
	12/7/18	Grt5	I1	0.84	2.38	0.93	2.56	-0.97	-0.79	0.91	2.53	1.00	2.70
	12/5/18	Grt6	I1	0.83	2.36	0.86	2.42	-1.14	-0.49	0.93	2.55	1.06	2.81
	12/7/18	Grt7	I1	0.81	2.33	0.86	2.42	-1.09	-0.54	0.91	2.52	1.03	2.75
	6/13/18	Grt8	I2	0.81	2.33	0.80	2.31	-1.50	0.11	0.96	2.62	1.18	3.05
	11/22/18	Grt9	I2	0.80	2.31	0.88	2.47	-1.08	-0.55	0.90	2.50	1.01	2.72
	11/22/18		I1	0.91	2.53	1.00	2.69	-1.07	-0.81	0.98	2.66	1.09	2.89
	11/22/18	Grt10	I2	0.85	2.41	0.89	2.48	-1.21	-0.45	0.96	2.61	1.10	2.89
	11/22/18	Grt11	I1	0.93	2.56	1.00	2.70	-1.10	-0.80	1.00	2.69	1.12	2.93
	non-ideal inclusions												
	6/13/18		I4	0.79	2.30	0.84	2.39	-1.29	-0.44	1.01	2.71	1.17	3.04
	6/13/18	Grt2	I7	0.57	1.91	0.64	2.03	-0.89	-0.30	0.69	2.11	0.77	2.26
	12/7/18	Grt4	I3	0.97	2.63	1.09	2.87	-1.05	-0.97	1.02	2.74	1.13	2.95
	12/5/18	Grt6	I2	0.98	2.65	1.02	2.73	-1.22	-0.71	1.05	2.79	1.19	3.10
	11/22/18		I1	0.98	2.65	1.08	2.87	-1.20	-0.74	1.05	2.80	1.19	3.08
	11/22/18	Grt9	I3	0.99	2.68	1.05	2.80	-1.22	-0.75	1.06	2.82	1.20	3.11
	11/22/18	Grt10	I3	0.95	2.59	1.03	2.75	-1.09	-0.86	1.01	2.72	1.13	2.95
	11/22/18	Grt11	I2	0.95	2.59	1.02	2.74	-1.19	-0.71	1.03	2.75	1.16	3.03

Note: Principal stress components and values of P_{inc} have been calculated from the strains using the full elastic tensor by Wang et al. (2015) as described in the text. P_{trap} values have been calculated using EosFit- P_{inc} (Angel et al., 2017). Non-ideal inclusions exhibit significantly different values of both P_{inc} and P_{trap} .

6.5 Conclusions

Prior to this study, it was not clear how the elastic anisotropy of quartz might affect the estimates of entrapment pressure of inclusions calculated by using a hydrostatic and isotropic model for host-inclusion systems. Our experimental results, summarized in Figs. 6.4 and 6.6, clearly show that the P_{inc} and P_{trap} values inferred from the hydrostatic calibration of the shift of the 464 cm^{-1} Raman line are in substantial error when the inclusions are subject to strains that are significantly different from those of a crystal under hydrostatic stress. Similarly, the P_{inc} and P_{trap} values calculated from the volume strain are systematically overestimated, because the inclusions are under non-hydrostatic stress. Therefore, the determination of P_{inc} as a mean stress derived from the strains determined from the measurement of several Raman lines is much more reliable. Second, the fact that our calculated $P_{\text{trap}}^{\text{strains}}$ values based on these measured $P_{\text{inc}}^{\text{strains}}$ are in good agreement with the experimental pressure of synthesis indicates that the effects of elastic anisotropy of quartz on the calculation from P_{inc} to P_{trap} is smaller than the other experimental uncertainties.

The level of apparent deviatoric stress ($\sigma_1 - \sigma_3$) in some of the inclusions of experiment Alm-1 is far greater than expected for quartz inclusions trapped in garnets under hydrostatic conditions (see, for example, Fig. 1 in Murri et al. (2018)). It is not clear whether these stresses are real, which might indicate the development of non-hydrostatic conditions in the piston-cylinder press, or simply an artifact arising from the strong correlation of the strains when determined from the positions of the Raman bands (Fig. 6.5).

Our experiments show that in order to obtain reliable estimates of P_{trap} of quartz inclusions, a number of steps are required. First, it is important to select approximately spherical inclusions for which the shape effects are

small and can be corrected (Mazzucchelli et al., 2018). Second, the inclusions must be isolated. Table 6.3a shows that partially-exposed inclusions (e.g. Grt2_I2) have partially-released stresses (Campomenosi et al., 2018; Mazzucchelli et al., 2018) and the resulting P_{trap} values can be up to 0.8 GPa too small for inclusions entrapped in our experiments at 3 GPa. On the other hand, inclusions that are close to other inclusions (e.g. Grt6_I1 in Table 6.3a) can exhibit inclusion stresses that are higher than isolated inclusions, and thus give P_{trap} values that are significantly too high. Once suitable inclusions have been identified the Raman shifts of several Raman lines from the inclusion must be measured as precisely as possible. This requires that a reference Raman spectrum is measured at the same time with the same instrument settings from a free quartz crystal in air. The strains in the inclusion should be determined from the changes in Raman shifts by using the mode Grüneisen tensors of quartz (Murri et al., 2018; Angel et al., 2019). The P_{inc} should then be calculated from these strains as the mean stress via the room-pressure elastic tensor of quartz (e.g. Wang et al., 2015). This P_{inc} can then be used in calculations based on the isotropic model for the evolution of host-inclusion systems (e.g. Angel et al., 2017) to calculate reliable P_{trap} values. The intrinsic uncertainties and the correlation in the strains obtained in this way (e.g. Fig. 6.5) suggest that multiple measurements of a population of quartz inclusions trapped under the same conditions are required to obtain a statistically reliable estimate of P_{trap} (as in Fig. 6.6).

6.6 Supplementary materials

Table 6.7: Composition of oxides mixture used to synthesize garnet with quartz inclusions and oxide mixture used for the fayalite-magnetite-quartz buffer

	oxide	wt%
starting material (QuiG 13-02-16)	SiO ₂	59,23
	Al ₂ O ₃	15,39
	FeO	10,1
	Fe ₂ O ₃	8,13
	TiO ₂	7,16
	MnO	0
FMQ	SiO ₂	23,43
	FeO	38,59
	Fe ₃ O ₄	37,98

Table 6.8: Raman peak positions of quartz reference crystals and their estimated standard deviations (*e.s.d.*). These values are the reference for calculating the change in Raman shift of the quartz inclusions in garnet (see Tables 6.1 and 6.2). For each day of measurements we used a single reference to determine Raman shifts between inclusions and quartz reference because the uncertainties of fitted peak positions is less than the instrumental accuracy in peak positions of $\sim 0.52 \text{ cm}^{-1}$.

	Date	Standard	Sample	location	128 (cm^{-1})	e.s.d	206 (cm^{-1})	e.s.d	464 (cm^{-1})	e.s.d
ALM-1	12-06-18	quartz thin section	THIN SECTION	eclogitic_ Fjordorf	127.235	0.038	205.962	0.046	464.072	0.016
	27-11-18	quartz thin section	THIN SECTION	granite_ Ivrea Verbano Zone	127.985	0.021	207.236	0.064	464.910	0.006
	05-12-18	quartz free crystal	FREE CRYSTAL	unknown	127.617	0.026	206.954	0.066	464.702	0.006
ALM-2	13-06-18	quartz thin section	THIN SECTION	Eclogitic_ Fjordorf	126.648	0.023	205.319	0.036	463.480	0.009
	22-11-18	quartz thin section	THIN SECTION	granite- Ivrea Verbano Zone	127.969	0.019	207.311	0.059	464.790	0.010
	05-12-18	quartz free crystal	FREE CRYSTAL	unknown	127.870	0.023	206.883	0.055	464.781	0.006

Table 6.9: Representative chemical composition of synthetic almandine host crystals by EMPA analysis.

experiment host n. analysis	Alm-1 Grt2 1	Alm-1 Grt2 2	Alm-1 Grt2 3	Alm-1 Grt6 1	Alm-1 Grt6 2	Alm-1 Grt6 3	Alm-1 Grt5 1	Alm-1 Grt5 2	Alm-1 Grt5 3	Alm-1 Grt5 4	Alm-1 Grt5 5	Alm-2 Grt4 1	Alm-2 Grt4 2	Alm-2 Grt4 3	Alm-2 Grt4 4	Alm-2 Grt4 5	Alm-2 Grt4 6	Alm-2 Grt4 7	Alm-2 Grt8 1	Alm-2 Grt8 2	Alm-2 Grt8 3	Alm-2 Grt8 4	Alm-2 Grt8 5
Al ₂ O ₃	21.410	20.940	22.090	21.460	21.580	21.050	21.630	20.880	20.590	21.500	20.940	21.640	20.090	20.720	21.320	21.300	21.090	20.830	21.590	21.420	20.960	21.560	21.110
SiO ₂	36.280	36.320	36.160	35.570	36.090	36.710	36.760	37.210	35.950	36.950	36.000	36.280	35.800	35.990	36.990	36.450	35.920	36.050	36.530	36.660	36.490	36.810	36.990
TiO ₂	0.877	1.098	1.076	0.913	1.105	0.924	0.666	0.815	1.136	0.526	1.233	0.528	0.885	0.921	0.593	0.616	0.706	0.849	0.745	0.607	0.944	0.463	0.596
FeO	44.650	44.600	44.350	44.250	44.810	44.200	43.970	44.920	44.820	44.370	45.040	44.400	45.350	45.870	44.540	44.320	45.280	45.480	44.470	43.940	44.950	44.890	45.120
Total	103.217	102.958	103.676	102.193	103.585	102.884	103.026	103.825	102.496	103.346	103.213	102.848	102.125	103.501	103.443	102.686	102.996	103.209	103.335	102.627	103.344	103.723	103.816
Al ₂ O ₃	2.031	1.993	2.082	2.058	2.042	1.998	2.046	1.967	1.974	2.030	1.994	2.058	1.941	1.975	2.013	2.028	2.015	1.987	2.042	2.035	1.989	2.033	1.991
SiO ₂	2.921	2.933	2.891	2.895	2.897	2.957	2.950	2.974	2.925	2.960	2.908	2.927	2.935	2.911	2.963	2.945	2.911	2.918	2.931	2.956	2.938	2.945	2.961
TiO ₂	0.053	0.067	0.065	0.056	0.067	0.056	0.040	0.049	0.070	0.032	0.075	0.032	0.055	0.056	0.036	0.037	0.043	0.052	0.045	0.037	0.057	0.028	0.036
FeO	3.006	3.012	2.966	3.012	3.009	2.977	2.951	3.003	3.050	2.972	3.043	2.996	3.109	3.103	2.984	2.994	3.069	3.079	2.984	2.962	3.027	3.004	3.020
sum	8.011	8.004	8.003	8.020	8.015	7.988	7.987	7.993	8.018	7.994	8.020	8.012	8.040	8.045	7.995	8.004	8.038	8.036	8.003	7.990	8.010	8.010	8.008
Oxygen	12	12	12	12	12	12	12	12	12	12	12	12	12	12	12	12	12	12	12	12	12	12	12

Weight percentage of oxides and sum of cations are normalized to a formula of 12 oxygens.

Chapter 7

Conclusions

During my PhD we developed two synthesis and calculation protocols pairs to validate the elastic geobarometry method for host-inclusion systems. The solid-state syntheses results are still incomplete, but we are now capable of producing suitable host-inclusion pairs that could be used to validate the elastic geobarometry approach. Hydrothermal syntheses have been very successful because we did produce suitable host-inclusion pairs for which the pressures determined using elastic barometry on the selected inclusions match those at which the synthesis were performed thus validating the elastic barometric method here adopted. The solid-state experiments have been extremely challenging as most of the protocols did not exist for these types of materials. Nonetheless we had the opportunity to explore some growth and transformation processes occurring very rapidly at modest P and T . The growth process is basically suppressed by using crystalline powder with micrometric size. The process could certainly be improved significantly at higher temperature, nevertheless the time to grow suitable sized grains would be too long to have significantly large single crystals. Therefore, we switched replaced the crystalline powder with more reactive non-crystalline powder.

This has improved the quality of the host. However, we remained with fundamental issues regarding the stoichiometric proportions of the reactant that considering the reactivity of non-crystalline powders can cause very easily the production of multiple other phases. The experiments with diamond as inclusions also allowed us to partly investigate the kinetic and shed light onto the mechanism of formation for graphite pseudomorphs after diamond. In all these experiments with diamond inserted as inclusions in garnet we obtained the typical cuboidal pseudomorph graphite after diamond. All diamonds completely transformed into graphite in less than 24 hours. The reaction occurs extremely fast (complete conversion from graphite to diamond in few minutes) as already shown by Kennedy and Kennedy (1976). Recently Korsakov et al. (2019) found cuboidal graphite in natural rocks and suggests that their formation is not related to the diamond-graphitization processes but can be ascribed to graphite precipitation from fluid or melt. Conversely, our experiments indicate that cuboidal graphite can also be formed also by complete graphitization without in absence of fluid or melt. Another important observation from these experiments regards the graphite plugs that allowed us to compensate part of the stresses produced during depressurization and quenching highlighting also that slow steady temperature decrease is not the only essential factor to retrieve uncracked crystals as proposed by Tingle (1988).

On the other hand, the hydrothermal synthesis allowed us to obtain a high quality of host-inclusion pairs. In a piston cylinder apparatus we synthesized two set of samples, *Alm-1* and *Alm-2* at $P=3.0$ GPa and $T=775$ °C and at $P=2.5$ GPa and $T=800$ °C, respectively. This method has the advantage that from one experiment we could produce a large number of garnet host crystal with trapped several inclusions, so we could retrieve stat-

istical information on reliability of elastic measurements on inclusions by means micro-Raman Spectroscopy. The disadvantage is that the inclusions are too small and too clustered to be measured using X-ray diffraction. On the selected inclusions after micro-Raman measurement and spectra fitting we determined the pressure on the inclusion using two different approaches (hydrostatic calibration and Grüneisen tensors) to assess the reliability of the results. The use of a hydrostatic calibration of the 464 cm⁻¹ line of quartz leads to a large spread in entrapment ‘pressure’ values that increase with increasing entrapment pressure conditions. For example, the errors on the entrapment pressure are about 1.4 GPa for inclusions synthesized at 3 GPa and approximately 0.2 GPa those synthesized at 2.5 GPa. These discrepancies arise mostly from the incorrect assumption of perfectly hydrostatic conditions that cannot be applied to elastically anisotropic inclusion trapped in a cubic host. Conversely, the use of the mode Grüneisen tensors for the quartz inclusions enables the full strain state of the inclusion to be determined from which its’ stress state can be calculated (Murri et al., 2018; Angel et al., 2019). Such a procedure leads to a much smaller spread in “pressure” values inferred for the inclusions; the maximum deviation from the experimental synthesis pressures is smaller than ± 0.2 GPa. The entrapment pressures calculated from the residual pressure obtained adopting the mode Grüneisen tensors approach is always higher than those obtained using the hydrostatic calibration. We demonstrated for the first time that the discrepancies between the results obtained with our protocol and those obtained with previously proposed methods are mainly caused by wrong assumption regarding the elastic anisotropy of the pair. The most significant result of this study is that the elastic anisotropy of quartz influence the calculation of entrapment pressure (P_{trap}) of inclusions.

Bibliography

- Adams, H. G., L. H. Cohen and J. L. Rosenfeld (1975). “Solid inclusion piezothermometry II: Geometric basis, calibration for the association quartz—garnet, and application to some pelitic schists”. In: *American Mineralogist: Journal of Earth and Planetary Materials* 60.7-8, pp. 584–598.
- Alvaro, M, M. Mazzucchelli, R. Angel, M Murri, N Campomenosi, M Scambelluri, F Nestola, A Korsakov, A. Tomilenko, F Marone et al. (2019). “Fossil subduction recorded by quartz from the coesite stability field”. In: *Geology*.
- Angel, R. and L. Finger (2011). “SINGLE: a program to control single-crystal diffractometers”. In: *Journal of Applied Crystallography* 44.1, pp. 247–251.
- Angel, R., M Alvaro, F Nestola and M. Mazzucchelli (2015a). “Diamond thermoelastic properties and implications for determining the pressure of formation of diamond-inclusion systems”. In: *Russian Geology and Geophysics* 56.1-2, pp. 211–220.
- Angel, R., P Nimis, M. Mazzucchelli, M Alvaro and F Nestola (2015b). “How large are departures from lithostatic pressure? Constraints from host-inclusion elasticity”. In: *Journal of Metamorphic Geology* 33.8, pp. 801–813.

- Angel, R. J., M. Alvaro and J. Gonzalez-Platas (2014a). “EosFit7c and a Fortran module (library) for equation of state calculations”. In: *Zeitschrift für Kristallographie-Crystalline Materials* 229.5, pp. 405–419.
- Angel, R. J., M. L. Mazzucchelli, M. Alvaro, P. Nimis and F. Nestola (2014b). “Geobarometry from host-inclusion systems: the role of elastic relaxation”. In: *American Mineralogist* 99.10, pp. 2146–2149.
- Angel, R. J., M. L. Mazzucchelli, M. Alvaro and F. Nestola (2017). “EosFit-Pinc: A simple GUI for host-inclusion elastic thermobarometry”. In: *American Mineralogist* 102.9, pp. 1957–1960.
- Angel, R. J., M. Murri, B. Mihailova and M. Alvaro (2019). “Stress, strain and Raman shifts”. In: *Zeitschrift für Kristallographie-Crystalline Materials* 234.2, pp. 129–140.
- Anzolini, C., M. Prencipe, M. Alvaro, C. Romano, A. Vona, S. Lorenzon, E. M. Smith, F. E. Brenker and F. Nestola (2018). “Depth of formation of super-deep diamonds: Raman barometry of CaSiO₃-walstromite inclusions”. In: *American Mineralogist* 103.1, pp. 69–74.
- Ashley, K. T., M. Steele-MacInnis, R. J. Bodnar and R. S. Darling (2016). “Quartz-in-garnet inclusion barometry under fire: Reducing uncertainty from model estimates”. In: *Geology* 44.9, pp. 699–702.
- Barron, T., J. Collins and G. White (1980). “Thermal expansion of solids at low temperatures”. In: *Advances in Physics* 29.4, pp. 609–730.
- Biggar, G. and M. O’hara (1969). “A comparison of gel and glass starting materials for phase equilibrium studies”. In: *Mineralogical Magazine* 37.286, pp. 198–205.
- Bonazzi, M., S. Tumati, J. B. Thomas, R. J. Angel and M. Alvaro (2019). “Assessment of the reliability of elastic geobarometry with quartz inclusions”. In: *Lithos* 350, p. 105201.

- Bose, K. and J. Ganguly (1995). "Quartz-coesite transition revisited: Reversed experimental determination at 500-1200 °C and retrieved thermochemical properties". In: *American Mineralogist* 80.3-4, pp. 231–238.
- Bower, A. F. (2009). *Applied mechanics of solids*. CRC press.
- Boyd, F. and J. England (1960a). "Apparatus for phase-equilibrium measurements at pressures up to 50 kilobars and temperatures up to 1750° C". In: *Journal of Geophysical Research* 65.2, pp. 741–748.
- (1960b). "The quartz-coesite transition". In: *Journal of Geophysical Research* 65.2, pp. 749–756.
- Bridgman, P. W. (1926). "The effect of pressure on the viscosity of forty-three pure liquids". In: *Proceedings of the American Academy of Arts and Sciences*. Vol. 61. 3. JSTOR, pp. 57–99.
- Campomenosi, N., M. L. Mazzucchelli, B. Mihailova, M. Scambelluri, R. J. Angel, F. Nestola, A. Reali and M. Alvaro (2018). "How geometry and anisotropy affect residual strain in host-inclusion systems: Coupling experimental and numerical approaches". In: *American Mineralogist* 103.12, pp. 2032–2035.
- Cantrell Jr, J. H. (1980). "Generalized Grüneisen tensor from solid nonlinearity parameters". In: *Physical review B* 21.10, p. 4191.
- Chopin, C. (1984). "Coesite and pure pyrope in high-grade blueschists of the Western Alps: a first record and some consequences". In: *Contributions to Mineralogy and Petrology* 86.2, pp. 107–118.
- Compagnoni, R. and T. Hirajima (2001). "Superzoned garnets in the coesite-bearing Brossasco-Isasca Unit, Dora-Maira massif, Western Alps, and the origin of the whiteschists". In: *Lithos* 57.4, pp. 219–236.

- Dobrzhinetskaya, L., S. Faryad and G. Hoinkes (Jan. 2013). “Mineral transformations in HP–UHP metamorphic terranes”. In: *Journal of Metamorphic Geology* 31.
- Edgar, A. D., A. D. Edgar et al. (1973). *Experimental petrology: basic principles and techniques*. Oxford: Clarendon Press.
- Enami, M., T. Nishiyama and T. Mouri (2007). “Laser Raman microspectrometry of metamorphic quartz: A simple method for comparison of metamorphic pressures”. In: *American Mineralogist* 92.8-9, pp. 1303–1315.
- Eshelby, J. D. (1957). “The determination of the elastic field of an ellipsoidal inclusion, and related problems”. In: *Proceedings of the Royal Society of London. Series A. Mathematical and Physical Sciences* 241.1226, pp. 376–396.
- Fyfe, W. (1960). “Hydrothermal synthesis and determination of equilibrium between minerals in the subliquidus region”. In: *The Journal of Geology* 68.5, pp. 553–566.
- (1961). “Problems and Progress in current research”. In: *Semicentennial publications* 59.5, pp. 553–566.
- Fyfe, W., F. Turner and J. Verhoogen (1958). “Metamorphic reactions and metamorphic facies: Geol”. In: *Soc. America Mem* 73, p. 259.
- Goodier, J. (1933). “Concentration of stress around spherical and cylindrical inclusions and flaws”. In: *Journal of Applied Mechanics* 55, pp. 39–44.
- Grüneisen, E (1926). “Zustand des festen Körpers”. In: *Thermische Eigenschaften der Stoffe*. Springer, pp. 1–59.
- Howell, D., I. Wood, D. Dobson, A. Jones, L. Nasdala and J. Harris (2010). “Quantifying strain birefringence halos around inclusions in diamond”. In: *Contributions to Mineralogy and Petrology* 160.5, pp. 705–717.

- Howell, D., I. G. Wood, F. Nestola, P. Nimis and L. Nasdala (2012). "Inclusions under remnant pressure in diamond: a multi-technique approach". In: *European Journal of Mineralogy* 24.4, pp. 563–573.
- Ikesue, A and Y. L. Aung (2006). "Synthesis and performance of advanced ceramic lasers". In: *Journal of the American Ceramic Society* 89.6, pp. 1936–1944.
- Irifune, T. and E. Ohtani (1986). "Melting of pyrope $\text{Mg}_3\text{Al}_2\text{Si}_3\text{O}_{12}$ up to 10 GPa: Possibility of a pressure-induced structural change in pyrope melt". In: *Journal of Geophysical Research: Solid Earth* 91.B9, pp. 9357–9366.
- Izraeli, E., J. Harris and O. Navon (1999). "Raman barometry of diamond formation". In: *Earth and Planetary Science Letters* 173.3, pp. 351–360.
- Jakobsson, S. (2012). "Oxygen fugacity control in piston-cylinder experiments". In: *Contributions to Mineralogy and Petrology* 164.3, pp. 397–406.
- Kennedy, C. S. and G. C. Kennedy (1976). "The equilibrium boundary between graphite and diamond". In: *Journal of Geophysical Research* 81.14, pp. 2467–2470.
- Kitahara, S and G. Kennedy (1964). "The quartz-coesite transition". In: *Journal of Geophysical Research* 69.24, pp. 5395–5400.
- Korsakov, A. V., O. V. Rezvukhina, J. A. Jaszczak, D. I. Rezvukhin and D. S. Mikhailenko (2019). "Natural Graphite Cuboids". In: *Minerals* 9.2, p. 110.
- Mazzucchelli, M. L., P. Burnley, R. J. Angel, S. Morganti, M. Domeneghetti, F. Nestola and M. Alvaro (2018). "Elastic geothermobarometry: Corrections for the geometry of the host-inclusion system". In: *Geology* 46.3, pp. 231–234.

- Mazzucchelli, M., A Reali, S Morganti, R. Angel and M Alvaro (2019). “Elastic geobarometry for anisotropic inclusions in cubic hosts”. In: *Lithos* 350, p. 105218.
- Milani, S, F Nestola, M Alvaro, D Pasqual, M. Mazzucchelli, M. Domeneghetti and C. Geiger (2015). “Diamond–garnet geobarometry: The role of garnet compressibility and expansivity”. In: *Lithos* 227, pp. 140–147.
- Miletich, R. (2005a). *Mineral Behaviour at Extreme Conditions*. Vol. 7. The Mineralogical Society of Great Britain and Ireland.
- (2005b). *Mineral Behaviour at Extreme Conditions*. Vol. 7. The Mineralogical Society of Great Britain and Ireland.
- Murri, M, M Alvaro, R. Angel, M Prencipe and B. Mihailova (2019). “The effects of non-hydrostatic stress on the structure and properties of alpha-quartz”. In: *Physics and Chemistry of Minerals* 46.5, pp. 487–499.
- Murri, M., M. L. Mazzucchelli, N. Campomenosi, A. V. Korsakov, M. Prencipe, B. D. Mihailova, M. Scambelluri, R. J. Angel and M. Alvaro (2018). “Raman elastic geobarometry for anisotropic mineral inclusions”. In: *American Mineralogist* 103.11, pp. 1869–1872.
- Nagira, T., H. Yasuda, T. Sakimura and K. Yoshida (2012). “Solidification of Al₂O₃–YAG eutectic composites with off-metastable eutectic composition from undercooled melt produced by melting Al₂O₃–YAP eutectics”. In: *Journal of the European Ceramic Society* 32.10, pp. 2137–2143.
- Nasdala, L, R. Pidgeon, D Wolf and G Irmer (1998). “Metamictization and U-Pb isotopic discordance in single zircons: a combined Raman microprobe and SHRIMP ion probe study”. In: *Mineralogy and Petrology* 62.1-2, pp. 1–27.
- Nestola, F., P. Nimis, L. Ziberna, M. Longo, A. Marzoli, J. W. Harris, M. H. Manghnani and Y. Fedortchouk (2011). “First crystal-structure determin-

- ation of olivine in diamond: Composition and implications for provenance in the Earth's mantle". In: *Earth and Planetary Science Letters* 305.1-2, pp. 249–255.
- Nye, J. *Physical Properties of Crystals*, (1957), 142.
- O'Brien, P. (2008). "Challenges in high-pressure granulite metamorphism in the era of pseudosections: reaction textures, compositional zoning and tectonic interpretation with examples from the Bohemian Massif". In: *Journal of Metamorphic Geology* 26.2, pp. 235–251.
- Richerson, D. W. (2005). *Modern ceramic engineering: properties, processing, and use in design*. CRC press.
- Rosenfeld, J. L. and A. B. Chase (1961). "Pressure and temperature of crystallization from elastic effects around solid inclusions in minerals?" In: *American Journal of Science* 259.7, pp. 519–541.
- S. Rezende, M. V. dos (2014). "Pressure dependence of dielectric constant, elastic constants, and lattice parameters of the Y₃(Ga,Al)O₁₂ host". In: *Journal of Physics and Chemistry of Solids* 75.10, pp. 1113–1118.
- Sanloup, C., B. C. Schmidt, E. M. C. Perez, A. Jambon, E. Gregoryanz and M. Mezouar (2005). "Retention of xenon in quartz and Earth's missing xenon". In: *Science* 310.5751, pp. 1174–1177.
- Schmidt, C. and M. A. Ziemann (2000). "In-situ Raman spectroscopy of quartz: A pressure sensor for hydrothermal diamond-anvil cell experiments at elevated temperatures". In: *American Mineralogist* 85.11-12, pp. 1725–1734.
- Shaw, C. S. (2018). "Igneous Rock Associations 22. Experimental Petrology: Methods, Examples, and Applications". In: *Geoscience Canada*, pp. 67–84.

- Simon, G., C. Chopin and V. Schenk (1997). “Near-end-member magnesiochloritoid in prograde-zoned pyrope, Dora-Maira massif, western Alps”. In: *Lithos* 41.1-3, pp. 37–57.
- Spear, F. S., J. B. Thomas and B. W. Hallett (2014). “Overstepping the garnet isograd: a comparison of QuiG barometry and thermodynamic modeling”. In: *Contributions to Mineralogy and Petrology* 168.3, p. 1059.
- Štípská, P and R Powell (2005). “Constraining the P–T path of a MORB-type eclogite using pseudosections, garnet zoning and garnet-clinopyroxene thermometry: an example from the Bohemian Massif”. In: *Journal of Metamorphic Geology* 23.8, pp. 725–743.
- Thomas, J. B. and F. S. Spear (2018). “Experimental study of quartz inclusions in garnet at pressures up to 3.0 GPa: evaluating validity of the quartz-in-garnet inclusion elastic thermobarometer”. In: *Contributions to Mineralogy and Petrology* 173.5, p. 42.
- Tingle, T. N. (1988). “Retrieval of uncracked single crystals from high pressure in piston-cylinder apparatus”. In: *American Mineralogist* 73.9-10, pp. 1195–1197.
- Trail, D., E. B. Watson and N. D. Tailby (2012). “Ce and Eu anomalies in zircon as proxies for the oxidation state of magmas”. In: *Geochimica et Cosmochimica Acta* 97, pp. 70–87.
- Wang, J., Z. Mao, F. Jiang and T. S. Duffy (2015). “Elasticity of single-crystal quartz to 10 GPa”. In: *Physics and Chemistry of Minerals* 42.3, pp. 203–212.
- Watson, E, D Wark, J Price and J Van Orman (2002). “Mapping the thermal structure of solid-media pressure assemblies”. In: *Contributions to Mineralogy and Petrology* 142.6, pp. 640–652.

- Yang, W.-C., H. Ade and R. Nemanich (2004). “Stability and dynamics of Pt-Si liquid microdroplets on Si (001)”. In: *Physical Review B* 69.4, p. 045421.
- Zhang, J. and C. Herzberg (1994). “Melting of pyrope, $\text{Mg}_3\text{Al}_2\text{Si}_3\text{O}_{12}$, at 7–16 GPa”. In: *American Mineralogist* 79.5-6, pp. 497–503.
- Zhang, Y. (1998). “Mechanical and phase equilibria in inclusion–host systems”. In: *Earth and Planetary Science Letters* 157.3-4, pp. 209–222.

Acknowledgments

Foremost, I would express my gratitude to my advisor Prof. Matteo Alvaro, for helping me in the data interpretation, for the encouragement and for the support during my PhD.

I would like to thank Prof. Simone Tumiatì for all helping during my work.

I am also pleased to say thank you to Dr. Ross J Angel for important work during the drafting of the article.

A special thanks to the research team: Dr. Mattia Mazzucchelli, Mara Murri, Gabriele Zaffiro (Paccio), Hugo Van Schrojenstein Lantman, Marta Morana, Dr. Mattia Gilio and Prof. M. Chiara Domeneghetti.

A huge thank you to all my friend who put up during these three years: Giacomo Giron, Luca Blardone (Dudy), Marco Vanotti, Davide Berno, Fabio Caracciolo, Yuri Panara, Isabella Flores, Matteo Bruga, Stefania Corvò, Michele Perozzo, Silvia Tamburelli, Riccardo Inama, Chiara Palmintieri, Andrea Pancini, Clelia Canova, Stefano Pozzi, Fabio Pizzo, Michela Margaria, Lorenzo Guaschino

A special thanks to Antonio Langone he guided me during my master thesis and through my first step of academia.

I am also pleased to say thank you to Alberto Zanetti who who introduced me to geochemistry.

Also thanks to the two reviewers of my PhD thesis Fabrizio Nestola and Costanza Bonadiman

Finally, my gratitude goes to my brother and brother's wife and my nephew, that supported me from the beginning and to Camilla that I met at the end of my PhD travel, but who believed in me during this short time.

This project has received fundings from:

European Research Council under the European Union's Horizon 2020 research and innovation program grant agreements 714936;

MIUR-SIR (Ministry of Education, University and Research Scientific Independence of Young Researchers, Italy) grant MILE DEEP (Mineral Inclusion Elasticity for a New Deep Subduction Geobarometer; RBSI140351) to Matteo Alvaro.